

# Determining Ideal Fields for Epoch of Reionisation Science Using the 21 cm Line

E. Jong,<sup>1</sup> C. M. Trott,<sup>1</sup> C. D. Nunhokee,<sup>1,2</sup> and Q. Zheng<sup>3</sup>

<sup>1</sup>International Centre for Radio Astronomy Research, Curtin University, Bentley WA, Australia

<sup>2</sup>ARC Centre of Excellence for All-Sky Astrophysics in 3D (ASTRO 3D), Australia

<sup>3</sup>Shanghai Astronomical Observatory, Chinese Academy of Sciences, 80 Nandan Road, Shanghai, 200030, P. R. China

Author for correspondence: E. Jong, Email: eric.jong@postgrad.curtin.edu.au.

## Abstract

The upcoming Square Kilometre Array Low Frequency (SKA-Low) interferometer will have the required sensitivity to detect the 21 cm line from neutral hydrogen during the Epoch of Reionisation (EoR). In preparation, we investigated the suitability of different fields for EoR science with the 21 cm line, using existing observations of candidate fields from the Murchison Widefield Array (MWA). Various image and calibration metrics were extracted from archival MWA observations centred on  $z \sim 6.8$ . We explore the usefulness of these metrics and compare their behaviour between different fields of interest. In addition, a theoretical approach to quantifying the impact of different fields on the power spectrum is also provided. Gain uncertainties were calculated based on the positions of the calibrators within the beam. These uncertainties were then propagated into visibilities to produce cylindrical power spectra for various fields. Using these metrics in combination with the power spectra, we confirm that EoR0 (R.A. = 0 deg, Dec = -27.0 deg) is an ideal EoR field and discuss the interesting behaviour of other fields.

## 1. Introduction

From the Cosmic Dawn (CD,  $z \sim 30-10$ ) through the Epoch of Reionisation (EoR,  $z \sim 10-5.3$ ), the Universe underwent incredible change. During the CD, neutral hydrogen (HI) atoms that formed at Recombination start to collapse gravitationally and form the first luminous objects. These objects then re-ionised the HI that surrounded them and created “bubbles” of ionised hydrogen (HII) — the beginning of EoR.

Over time, with the formation of new luminous sources and bubbles continuously expanding, we arrive at the bright and mostly ionised Universe of the present day. Understanding the evolution of hydrogen helps to reveal the properties of the first stars, such as the processes involved in the formation of these stars, their mass, when they first formed, and how the Universe evolved from a smooth matter distribution to its complex structures of today (Furlanetto, Peng Oh, and Briggs 2006; Zheng et al. 2020; Koopmans et al. 2015). Evidently, there lies a wealth of knowledge crucial to our understanding of the Universe.

To trace neutral hydrogen, the 21 cm wavelength photon produced by the hyperfine transition in the ground state of hydrogen is of interest. This particular wavelength is not easily re-absorbed by other hydrogen atoms, hence it travels through the neutral hydrogen medium unimpeded. Although it may take multiple millions of years for a single hydrogen atom to produce this signal (Storey et al. 1994), the abundance of hydrogen ensures that we can probe these time periods. For a thorough review of the history of HI in the Universe, see Pritchard and Loeb 2012; Koopmans et al. 2015; Furlanetto, Peng Oh, and Briggs 2006 and references therein.

Major efforts in EoR science lie in measuring the brightness temperature of the 21 cm line at some particular redshift, through a variety of statistics; the brightness temperature spatial power spectrum is commonly used. This is undertaken through observations with radio interferometers such as the Murchison Widefield Array (MWA, Tingay et al. 2013; Wayth et al. 2018), LOw-Frequency Array (LOFAR, Haarlem et al. 2013), New Extension in Nançay Upgrading LOFAR (NENUFAR, Zarka et al. 2015), Hydrogen Epoch of Reionization Array (HERA, DeBoer et al. 2017), the Giant Metre-wave Radio Telescope (GMRT, Swarup et al. 1991), and the Long Wavelength Array (LWA, Ellingson et al. 2009). Results for the upper-limit on the 21 cm brightness temperature have also been reported by these instruments: MWA (Trott et al. 2020; Nunhokee et al. 2025), LOFAR (Mertens et al. 2020; Acharya et al. 2024; Mertens et al. 2025), NenuFAR (Munshi et al. 2024; Munshi et al. 2025), HERA (Abdurashidova et al. 2022; HERA Collaboration et al. 2023), GMRT (Paciga et al. 2011), and LWA (Eastwood et al. 2019).

There are many challenges in the measurement of the 21 cm signal. Radio signals from astrophysical and human sources produce foreground contamination; processes such as synchrotron emission, free-free scattering, bright radio sources, radio emission from digital television channels, FM radio emissions and satellites are orders of magnitude brighter than the 21 cm line (Bowman and Rogers 2010; Chapman and Jelić 2019; Offringa et al. 2015). Imprecise calibration solutions have also been a challenge in these experiments. Spectral features in the calibration solutions can propagate into the power spectra and affect our ability to make a measurement.

Spectral features caused by using an incomplete sky model in the calibration step (Barry *et al.* 2016; Ewall-Wice *et al.* 2017; Procopio *et al.* 2017) or errors in beam responses (Nunhokee *et al.* 2020; Chokshi *et al.* 2024; Brackenhoff *et al.* 2025) have been shown to overwhelm the feeble 21 cm signal. Clearly, the study of these processes is crucial to minimising their effect and for the success of EoR science.

This paper aims to investigate one such challenge, that is, how different parts of the sky impact data calibration and in turn determine the ideal fields of the sky for EoR observations with SKA-Low. The calibration is sensitive to different parts of the sky due to the density of sources, brightness distribution of sources, and the types of sources present (compact or extended).

The MWA collaboration has selected two regions of the sky which are deemed fit for EoR science: EoR0 (R.A. =  $0^\circ$ , Dec =  $-27^\circ$ ), and EoR1 (R.A. =  $60^\circ$ , Dec =  $-27^\circ$ ). EoR0 is described as containing a few, bright resolved sources allowing for “easier” calibration (Jacobs *et al.* 2016). EoR1 was chosen for similar reasons, containing another cold patch of the sky.

The LOFAR collaboration observes two main fields, the North Celestial Pole (NCP, Yatawatta *et al.* 2013), and 3C196 (Asad *et al.* 2015; Ceccotti *et al.* 2025). The NCP was selected (apart from the benefits due to the location of the interferometer) for its position in a relatively cold spot of the galactic halo, which reduces foregrounds, and because it did not contain an extremely bright source, which results in less artefacts from deconvolution. The 3C196 field was chosen due to its position in a colder region of the galactic halo and due to the presence of a very bright unresolved source located near the centre resulting in accurate direction-independent calibration.

The HERA collaboration, which uses a zenith pointed array, observes various fields throughout a large range of LSTs. Some fields were selected due to minimal diffuse foregrounds and the presence of a bright source from the GLEAM catalogue (Wayth *et al.* 2015; Abdurashidova *et al.* 2022). Additional fields were selected to avoid Fornax A and the galactic centre (HERA Collaboration *et al.* 2023).

More recently, candidate fields have been chosen by Zheng *et al.* 2020 for the upcoming SKA-Low, using a limited number of parameters to determine field quality, such as minimal galactic emission chosen by cool regions of the Haslam 408 MHz All-Sky map (Haslam *et al.* 1982), far from the Magellanic clouds, contain minimal bright radio sources that are uniformly positioned within the beam, and should not contain resolved radio diffuse sources. These parameters help to select fields with the intention of making the subsequent post-processing steps (foreground subtraction, calibration, and imaging) easier, and more accurate. Further processing and analysis of one of the candidate fields from this work, and several other “quiet” fields show that selecting a suitable field is critical for EoR science with the SKA (Zheng *et al.* in prep.).

In this work we extend those parameters, and also extend the number of fields studied. We take both a data-driven and a theoretical approach to this problem to determine the key parameters for determining the quality of a field for EoR science. We use observations of existing fields from the MWA telescope

and study the actual calibration precision. We also apply a theoretical approach to predict the most precise calibration that can be obtained for each field. This paper will focus on MWA parameters for characterising fields, but the applicability to the SKA-Low will also be discussed.

This paper is structured as follows, Section 2 goes through the details and process in obtaining data used in this work. Section 3 will discuss the theoretical aspects and desired behaviour of the chosen metrics in this work. Section 4 discusses the theory behind calculating the gain uncertainties. Section 5 describes the computational aspects of the work. In Section 6 we present the results for the extracted metrics and the theoretical gain uncertainties. In Section 7 we discuss and compare the results for the different fields, and finally we conclude the work in Section 8.

## 2. Data method

### 2.1 Murchison Widefield Array details

The MWA is a radio interferometer located at the Murchison Radio-Astronomy Observatory, a radio quiet zone in Western Australia (Tingay *et al.* 2013). In this work we are concerned with the phase II extended configuration (Wayth *et al.* 2018) of the telescope. This configuration contains 128 tiles with a maximum baseline of approximately 5.2 km. Its operating frequencies are from 70 MHz to 300 MHz, with a field of view of approximately 26 degrees at 150 MHz. The MWA produces data at a spectral resolution of 10 kHz, and a temporal resolution of 0.5 seconds. Each observation is typically 2 minutes in duration covering only a 30.72 MHz instantaneous bandwidth.

### 2.2 Data collection and pre-processing

Data were obtained from the MWA ASVO archive <sup>a</sup> through the MWA TAP service. The TAP service was queried with the following settings: observations are within a circle of radius  $5^\circ$  of the phase centre, and centred on channel 144 (184.32 MHz, which corresponds to  $z \sim 6.8$ ). With these settings, we obtain observations centred on one of two frequency bands designated for EoR. Furthermore, the settings allow us to obtain as many observations as we can without the sky changing significantly between observations. As mentioned earlier, these observations were made in the Phase II configuration, which allows us to extend upon EoR observations performed by Zheng *et al.* 2020.

In this work, we inspect the fields used by MWA (EoR0 and EoR1, Barry *et al.* 2019; Trott *et al.* 2020; Rahimi *et al.* 2021), fields which have been used by HERA (Abdurashidova *et al.* 2022), and fields which were chosen by other metrics (prefixed with “SKAEOR”, Zheng *et al.* 2020). The phase centres and number of observations for all the fields investigated are given in Table 1. A figure highlighting the fields on the radio sky is given in Figure 1. Due to the use of analog beamformers in the MWA, the interferometer is only capable of coarse pointing (Tingay *et al.* 2013). Thus, from the perspective of the MWA the sky is broken into certain “grid numbers” (also known as pointing numbers) which describe the pointing. For

a. <https://asvo.mwatelescope.org/>

each field, numerous observations are used, in order to separate field-based structure from poor observations (e.g., due to the health of the telescope itself).

**Table 1.** Table of fields which have been downloaded and processed, alongside the right ascension (deg) and declination (deg) of their phase centres. Listed are EoR0 and EoR1 (Lynch et al. 2021), fields used by HERA (Abdurashidova et al. 2022), and fields chosen by other metrics (prefixed with “SKAEOR”, Zheng et al. 2020)

| Field name   | RA (deg) | DEC (deg) | Num. obs. |
|--------------|----------|-----------|-----------|
| EoR0         | 0.00     | -30.00    | 55        |
| EoR1         | 60.00    | -30.00    | 35        |
| HERA LST 2.0 | 30.00    | -30.00    | 31        |
| HERA LST 5.2 | 78.00    | -30.00    | 86        |
| SKAEOR5      | 118.91   | 5.86      | 100       |
| SKAEOR6      | 128.40   | -3.52     | 26        |
| SKAEOR14     | 158.14   | -12.66    | 53        |
| SKAEOR15     | 72.5     | -13.35    | 100       |

Once the data had been downloaded, they were calibrated for direction-independent gains with Hyperdrive<sup>b</sup> (Jordan et al. 2025). The sky model used is a combination of different surveys and models, including LoBES (Lynch et al. 2021) for the EoR 0 field, Procopio et al. 2017 for the EoR1 field, Line et al. 2020 for a shapelets model of Fornax A, (Cook, Trott, and Line 2022) for the Centaurus A model and Galactic Plane Supernova Remnants, and the GLEAM survey (Wayth et al. 2015; Hurley-Walker et al. 2016). Only Stokes I information were used for the sky model. We used the brightest 8000 sources. In addition, Hyperdrive uses a per-channel calibration at the resolution of 2 s/40 kHz. Furthermore, Hyperdrive considers the leakage terms in the Jones matrix of the beam response, utilises a simulated Full Embedded Element (FEE) beam model (Sokolowski et al. 2017), and solves for calibration solutions per frequency channel using a similar process described by Mitchell et al. 2008. No antenna flagging algorithms were applied to the data.

Calibration solutions were assessed using the MWA’s Quality Analysis pipeline (Nunhokee et al. 2024). Amplitude calibration solutions were normalised to the median and the phase solutions were also unwrapped before calculating the metrics.

The calibrated visibilities were imaged with WSCLEAN (Offringa et al. 2014). Deconvolution (CLEAN, Högbom 1974) was applied until the data reached the  $3\sigma$  noise threshold or reached the maximum number of iterations (set to 10000). Since the field of view of the main lobe of the MWA beam is approximately 21 degrees at 184.32 MHz, we set scale of each pixel to 15 arcseconds and the image size to  $5064 \times 5064$  pixels.

### 3. Metrics

This work aims to provide a data driven approach to selecting ideal fields for EoR science. With this motivation, we will

explore the insight and usefulness of a variety of metrics in both the image and calibration space. The metrics to be discussed and their desired behaviour are given in Table 2.

**Table 2.** Table of metrics to be extracted from archival MWA data, and their desired behaviour.

| Metric                               | Desired behaviour |
|--------------------------------------|-------------------|
| Image root-mean-square noise         | Low               |
| Image dynamic range                  | High              |
| Calibration Gain smoothness          | Low               |
| Calibration Phase RMSE               | Low               |
| Calibration Phase MAD                | Low               |
| Calibration Phase Euclidean distance | Low               |
| Calibration Phase KS-metric          | Low               |

The following sections will first have a brief explanation for the motivation and expected behaviour, followed by more detailed discussion.

#### 3.1 Image Metrics

**Motivation:** Residual signal in peeled images indicates the presence of unmodelled source sidelobe.

**Expected behaviour:** Root-mean-square noise should be minimised and dynamic range maximised.

In this work, deconvolved multi-frequency-synthesis images are produced. Hence, residual signal in these images indicates the presence of unmodelled source sidelobes. The root-mean-square (RMS) and dynamic range (DR) are used to quantify the residual signal. The RMS should be minimised and DR maximised; a high RMS may completely obscure the 21 cm signal and may indicate significant contamination from source sidelobes, while a low DR indicates a lack of bright calibrators or, again, contamination from source sidelobes. The RMS and DR are calculated with the following equations

$$\sigma_{\text{rms}} = \sqrt{\frac{1}{N} \sum_i x_i^2} \quad (1)$$

and

$$\chi = \frac{X}{\sigma_{\text{rms}}} \quad (2)$$

respectively, where  $x_i$  is the value of each pixel,  $N$  is the number of pixels, and  $X$  is the value of the brightest pixel.

Deconvolving in the image plane is conceptually related to the process of peeling in the visibility plane: they both aim to remove unwanted sidelobes from the data. The peeling of visibilities is a common step in creating power spectra for EoR science, hence the RMS of deconvolved images can still be suitable for determining candidate EoR fields. However, in this work, the RMS metric is intended as a simple diagnostic to compare different fields. Therefore, it is most important to ensure consistency in how these images are generated.

b. [https://github.com/MWATelescope/mwa\\_hyperdrive](https://github.com/MWATelescope/mwa_hyperdrive)

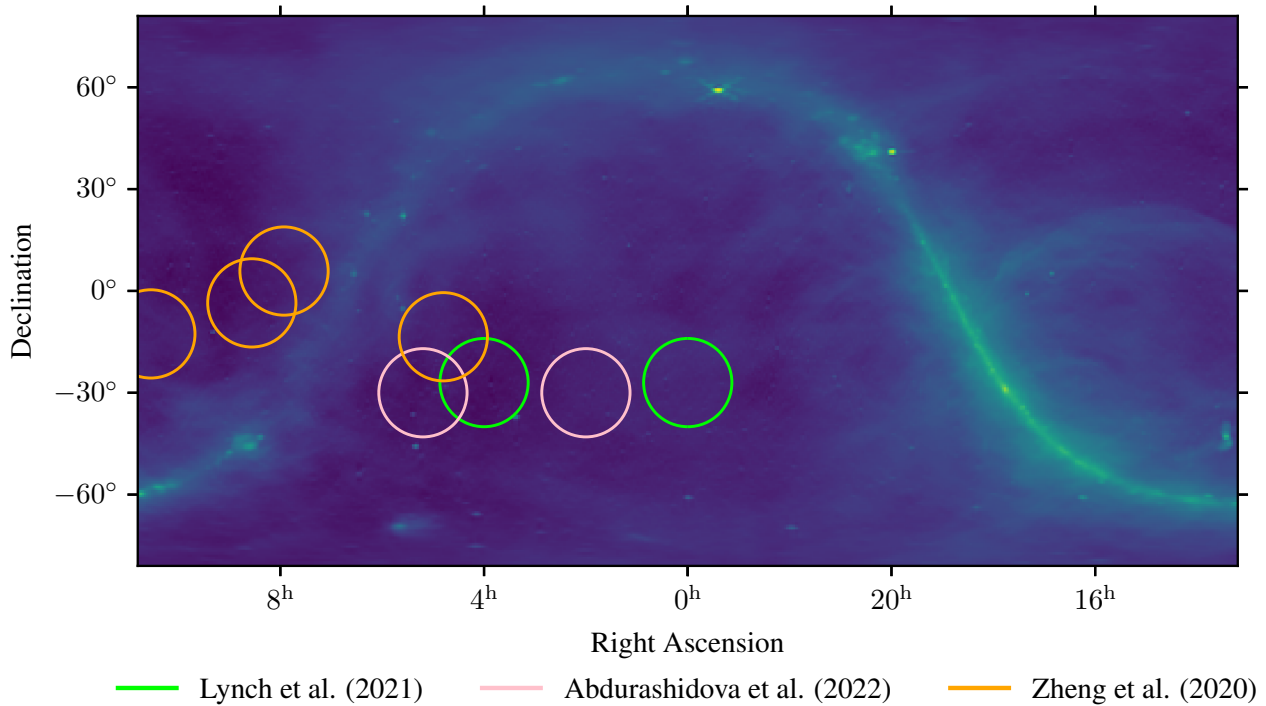


**Figure 1.** Fields of interest in this study highlighted on the 408 MHz all-sky map (Haslam et al. 1982). Highlighted in green are the MWA EoR1 and EoR2 fields (Lynch et al. 2021). In pink are HERA fields (Abdurashidova et al. 2022). In orange are fields selected by other metrics (Zheng et al. 2020).

### 3.2 Amplitude solutions smoothness

**Motivation:** Spectral features in gain amplitudes propagate into final statistics of interest.

**Expected behaviour:** Smoothness metric should be minimised.

In the calibration solutions case, we investigate the amplitude and phase of the calibration solutions separately. For the amplitude solutions we inspect the smoothness of the solutions across frequency. The smoothness is especially important since Hyperdrive, our calibration tool, makes no assumptions on how the complex gains should behave; Hyperdrive solves for solutions per-frequency, hence capturing most of the spectral features. In methods that use regularisation, assumptions about how the gains behave are made, and a penalty function is used to constrain the solutions (Ikeda et al. 2025; Yatawatta 2015) which may bias the solutions towards a certain class of solutions.

Amplitude solutions that are not smooth — which may be the result of the particular observing field or an error at the time of observation — can contain spectral structure due to a poor sky model which will propagate into the final power spectrum (Byrne et al. 2019; Ewall-Wice et al. 2017; Barry et al. 2016). This can heavily affect the ability to make a measurement, hence we suggest that smooth amplitude solutions are ideal. We calculate the smoothness of the amplitude solutions with the following

$$S = \frac{1}{M} \sum_{i=1}^{N_+} m_i, \quad (3)$$

where  $M$  is the value of the DC-mode of the Fourier Transform (FT) of the amplitude solutions,  $m_i$  is the value of the  $i$ -th positive Fourier mode (after normalising to the median), and  $N_+$  is the number of positive Fourier modes. Since the amplitude solutions are not a periodic signal, we also apply the Blackman-Harris window to reduce spectral leakage (Lessard 2006).

### 3.3 Phase solutions metrics

**Motivation:** Phase solutions should be linear and similar between the two polarisations.

**Expected behaviour:** Root-mean-square-error, mean-absolute-deviation, KS-test, and Average Euclidean distance should all be minimised.

Hyperdrive applies direction-independent calibration, meaning it calibrates for time delays in the system which arise from factors such as cable lengths from antenna to receiver. A time delay in the signal corresponds to a linear phase shift in Fourier space. Hence, we investigate the linearity of the phase solutions with the root-mean-square-error (RMSE) and mean-absolute-deviation (MAD). The RMSE and MAD are calculated using the following



$$\text{RMSE} = \sqrt{\frac{1}{N} \sum_1^N (x_i - \hat{x}_i)^2} \quad (4)$$

and

$$\text{MAD} = \frac{1}{N} \sum_1^N |r_i - R|, \quad (5)$$

where  $N$  is the number of frequency channels,  $x_i$  is the antenna's phase solution at frequency channel  $i$ ,  $\hat{x}_i$  is the phase solution predicted by the line of best fit,  $r_i$  are the residuals between the observed and predicted phase solutions and  $R$  is the mean value of the residuals.

Another intriguing aspect of the phase solutions arise from the fact that the NS and EW dipoles have differing response patterns. Hence, investigating the similarity between the NS and EW polarisation phase solutions may provide interesting insight in the behaviour of a field. Here, we suggest solutions which are similar to each other are better than those which are not similar. A dissimilarity can indicate bright sources are present in one polarisation and not the other, or suggest an error occurred during observation in one polarisation. We use two metrics to describe the similarity, the average Euclidean distance between the two sets of solutions, and the Kolmogorov-Smirnov (KS) metric. The Euclidean distance is simply the average of the distance between the NS and EW phase solutions at each channel. A smaller value indicates that the solutions are closer. The KS metric tests how similar the underlying empirical distribution functions of the two sets of solutions are, a value of 0 indicates the two sets are identical while a value of 1 indicates they are the most dissimilar.

#### 4. Theoretical method

In addition to the metrics, a theoretical approach was used to assess the information content of data from different fields and the consequent impact on calibration precision.

##### 4.1 Gain uncertainties

For the theoretical analysis of gain uncertainties, we have used the Cramér-Rao bound (CRB) statistic. The CRB provides a lower bound on the variance of an unbiased estimator; or, equivalently, it provides the precision of an unbiased estimator. It does not provide a method for estimating the unknown parameters. The CRB has been used previously to investigate the effects of imprecise calibrator parameters such as the position, spectral index, and brightness (Trott et al. 2011). In this work, the same methods were applied to investigate the best a calibration pipeline can estimate gain uncertainties.

We begin with the Fisher Information Matrix, an element of which can be written in the form (Kay 1993)

$$I_{ab}(\theta) = \frac{2}{\sigma^2} \int \frac{\partial s^H(t; \theta)}{\partial \theta_a} \frac{\partial s(t; \theta)}{\partial \theta_b} dt, \quad (6)$$

where  $\sigma^2$  is the variance,  $s(t; \theta)$  is a signal,  $H$  denotes the Hermitian conjugate, and  $\theta$  is a vector of unknown parameters which the signal is conditioned on. The signal is given by

$$V_{ab} = \sum_{j=1}^{N_c} B_j g_a \bar{g}_b \exp(-2\pi i(u_{ab} l_j + v_{ab} m_j)), \quad (7)$$

where  $g_a$  and  $g_b$  are the complex gains of antennas  $a$  and  $b$  respectively,  $u_{ab}$  and  $v_{ab}$  are the baseline coordinates between antennas  $a$  and  $b$ ,  $B_j$  is the brightness of calibrator  $j$ , and  $l_j$  and  $m_j$  are the calibrator's coordinates (direction cosines). In this study, we have assumed  $g_a = g_b = 1$ , i.e. unity gains.

We are concerned with how well we can estimate the gains  $g_a$  and  $g_b$ , hence for a telescope with  $N$  antennas we have  $\theta = [g_1, g_2, g_3, \dots, g_N]$ . This means  $s(t; \theta)$  in Equation 6 is a vector of visibilities measured by every baseline. Each element of this vector of length  $N_{\text{baselines}}$  is given by Equation 7, where  $N_{\text{baselines}} = N^2$  is the number of baselines, including conjugates, and auto-correlations to complete the matrix. Taking the partial derivative of this vector with respect to  $g_a$  we have

$$\frac{\partial s_{ab}(t; \theta)}{\partial g_a} = \sum_{j=1}^{N_c} B_j \bar{g}_b \exp(-2\pi i(u_{ab} l_j + v_{ab} m_j)). \quad (8)$$

This means most of the vector,  $\frac{\partial s(t; \theta)}{\partial g_a}$ , will possess a value of 0 and  $N$  elements will be populated, since  $N_{\text{baselines}} - N$  elements do not contain  $g_a$  and will be differentiated to 0.

When  $a \neq b$ , the product of the two partial derivatives is then only non-zero when the product contains  $g_a$  and  $g_b$ . For example, for antennas 1 and 2 the product is non-zero when the terms  $g_1$  and  $g_2$  are both present in the product. When  $a = b$ , the product of the partial derivatives is non-zero at  $N$  elements,  $N - 1$  of those elements are identical, and 1 element will have a multiplicative factor of 4 due to the partial derivative of a  $g_a^2$  term. Hence, when  $a = b$ , an additional multiplicative factor of  $N + 3$  is needed, this condition can be expressed with a Kronecker-delta function. The final expression for an element of the Fisher Information Matrix is

$$I_{ab}(\theta) = (N + 3) \delta_{ab} \times \frac{2}{\sigma^2} \times \int \sum_{j=1}^{N_c} \sum_{k=1}^{N_c} B_j B_k g_a \bar{g}_b \exp\{-2\pi i(u_{ab}(l_j - l_k) + v_{ab}(m_j - m_k))\} dt. \quad (9)$$

The variance  $\sigma^2$  of a single visibility signal measured by a single baseline is given by

$$\sigma = \frac{2k_b T_{\text{sys}}}{A_{\text{eff}} \sqrt{\Delta\nu \Delta\tau}}, \quad (10)$$

where  $k_b$  is the Boltzmann constant,  $T_{\text{sys}}$  is the system temperature,  $A_{\text{eff}}$  is the effective area of an antenna,  $\Delta\nu$  is the

bandwidth of a single measurement, and  $\Delta\tau$  is the integration time for a single measurement.

The CRB matrix is then the inverse of Equation 9, and the gain uncertainties can be found on the square-root of the diagonal of this matrix. Previous work with the CRB (Trott *et al.* 2011) has shown one bright calibrator produces better gain and phase precision compared to many lower brightness sources.

## 4.2 Propagation of gain uncertainties

To propagate gain uncertainties into the visibilities we use the standard covariance matrix method given by

$$\sigma_{V_{ab}}^2 = [\mathbf{J}\mathbf{C}_\theta\mathbf{J}^\dagger]_{ab}, \quad (11)$$

where  $\mathbf{J}$  is the Jacobian of partial derivatives of the visibility function with respect to the parameters  $\theta_{ab} = (g_a, g_b)$ ,  $\mathbf{J}^\dagger$  is the complex conjugate, and  $\mathbf{C}_\theta$  is the covariance matrix of parameter uncertainties. Expanding out equation 11, we arrive at the following

$$\begin{aligned} \sigma_{V_{ab}}^2 = & \left| \frac{\partial V_{ab}}{\partial g_a} \right|^2 \sigma_{g_a}^2 + \frac{\partial V_{ab}}{\partial g_a} \frac{\partial \overline{V_{ab}}}{\partial g_b} \text{cov}_{g_b g_a} \\ & + \frac{\partial \overline{V_{ab}}}{\partial g_a} \frac{\partial V_{ab}}{\partial g_b} \text{cov}_{g_a g_b} + \left| \frac{\partial V_{ab}}{\partial g_b} \right|^2 \sigma_{g_b}^2, \end{aligned} \quad (12)$$

and since we assume the gains are unity, meaning the coefficients of the variance and covariance terms are the same, this expression can be simplified further to

$$\sigma_{V_{ab}}^2 = \left| \frac{\partial V_{ab}}{\partial g_a} \right|^2 (\sigma_{g_a}^2 + \text{cov}_{g_a g_b} + \text{cov}_{g_b g_a} + \sigma_{g_b}^2). \quad (13)$$

The variance and covariance terms can be directly taken from the diagonal and off-diagonals of the CRB matrix, respectively.

## 5. Computational Method

### 5.1 Metrics

The evaluation of both the image and most of the calibration metrics is simple. Equations 1 and 2 were evaluated after reading in the image data. The smoothness of the amplitude solutions of the antenna were found by evaluating Equation 3, after applying a Blackman-Harris window to the solutions. The phase linearity metrics were evaluated for each set of phase solutions by first applying a linear fit to the data, then evaluating Equation 4 and Equation 5. The Euclidean distance was simply the average of the absolute value of the difference between the NS and EW phase solutions at each channel, and the KS metric was obtained using the `kstest` method from `scipy` (Virtanen *et al.* 2020).

### 5.2 Detecting metric outliers

It is inevitable that some observational data are corrupted by some source of error that is independent of the sky, such as problems with the telescope or strong RFI. For this work, these effects need to be disentangled from sky-based effects. Processing these bad observations will result in outliers in the metrics. These outliers were detected by first treating each observation's metrics as a 128-dimensional point then calculating the distance to every other observation's metrics (another 128-dimensional point). We then calculate the MAD for these distances to use in the modified z-score. In this paper, a threshold of  $5\sigma$  was used to determine if a result is an outlier. The number of observations left after applying this method for each field is given in Table 3.

**Table 3.** Number of 2-minute observations per field remaining after bad data have been removed with the method described in Section 5.2.

| Field name   | Num. observations |
|--------------|-------------------|
| EoR0         | 39                |
| EoR1         | 25                |
| HERA LST 2.0 | 19                |
| HERA LST 5.2 | 63                |
| SKAEOR5      | 65                |
| SKAEOR6      | 21                |
| SKAEOR14     | 28                |
| SKAEOR15     | 68                |

### 5.3 Gain uncertainties

In this work, all simulations are zenith pointed meaning simulations of some of the fields may not be representative of reality, as some fields do not transit the zenith of the MWA. However, this allows us to compare the effects of source positions within the beam between the different fields. Furthermore, it is common to calibrate only with sources within the main lobe of the primary beam, because these are the most reliable. Hence, during these calculations, only sources within the main lobe are preserved. The main lobe will change slightly depending on pointing, but overall it will behave similarly whether at zenith or off-zenith. Therefore, simulating at zenith will still provide valuable insight while allowing for much easier implementation.

Additionally, all components in the sky model are treated as point sources in the simulation, as Equation 9 requires only the brightness and positions of the sources. This means that Fornax A, which is composed of shapelets in our sky model, is modelled as a set of point sources with large brightness. Moreover, systematics like sky model uncertainties are unaccounted for; all other parameters are assumed to be accurate.

Equation 10 was first evaluated for the given input parameters. In this work the values used are representative of EoR science with the MWA telescope  $T_{\text{sys}} = 200$  K (value at the centre of the bandwidth),  $N = 128$ ,  $A_{\text{eff}} = 21$  m<sup>2</sup>,  $\Delta\nu = 80$  kHz, and  $\Delta\tau = 8$  s. The field of view of a telescope can be approxi-

mated with  $\theta \approx \frac{\lambda}{D}$  where  $D$  is the diameter of a dish/antenna. For the MWA,  $D = 4.4$  m. We have assumed that  $A_{\text{eff}}$  does not change with frequency (Tingay et al. 2013).

Next, the calculation and propagation of the gain uncertainties takes place within a large loop over the frequency behaviour could be due to sources moving in and out of the range. At the beginning of each iteration, sources in the sky/main/side lobes of the MWA with observation ID. Although model were vetoed by the current field of view and also these metrics are displayed in increasing observation ID, it estimated flux density for that frequency. Following this, the does not necessarily mean successive points are observations beam pattern is calculated for the current frequency, using performed immediately after each other. the array factor method (Warnick et al. 2018), in a 1024 by 1024 grid where each pixel corresponds to a portion of the sky in the  $(l, m)$  plane. These pixel values are used to attenuate sources located within the pixel by simply multiplying the source brightness by the pixel value.

The attenuated sources are then used to calculate the CRB matrix by first generating the FIM matrix with Equation 9, where each element represents an antenna pair  $(a, b)$ . The FIM is Hermitian, hence only the top triangle of the matrix needs to be calculated and the bottom triangle can be filled in by taking the complex conjugate. The CRB are the diagonal elements of the inverse of the FIM matrix, and the gain uncertainties for each antenna are their square-root.

#### 5.4 Power spectra

Taking the previously calculated gain uncertainties, still within the large frequency loop, the uncertainties for visibilities were evaluated with Equation 13. Once uncertainties were calculated, the real and complex components for the visibilities for each baseline were randomly generated from a normal distribution with mean 0 and standard deviation  $\frac{\sigma_{V_{ab}}}{\sqrt{2}}$ . The visibilities were then gridded onto a common  $(u, v)$  grid, and appended onto a growing list of gridded visibilities.

Once the loop completed, we were left with a data cube of gridded visibilities at each frequency channel. To transform this data cube into the final power spectrum, a Fourier Transform was applied to each  $(u, v)$  cell along the frequency axis. The result was then multiplied by its complex conjugate to yield the unnormalised power. We then cylindrically average the unnormalised power at each  $\eta$  slice (the FT of frequency) to arrive at the 2D temperature power spectrum.

## 6. Results

This section will present the results of the calculations and attempt to provide explanations for the behaviour seen in some metrics. The information gained and the usefulness of the metrics will also be discussed. All results shown are generated after applying the threshold technique discussed in Section 5.2. Outliers in this study generally stem from either computational errors or bad data, not from the behaviour of the fields.

Differences between NS and EW polarisations arise from their different fringe patterns. In this section, we display results only for the EoR0 field as an indicative field; results for the others can be found in the appendices. The following metrics were found to be most useful: image RMS and dynamic range, amplitude smoothness, and phase RMSE.

#### 6.1 Image metrics

The RMS and dynamic range of the EoR0 field can be found in Figure 2. Both the RMS and DR of the fields can be seen varying with the observation ID for a particular pointing. This behaviour could be due to sources moving in and out of the range. Although these metrics are displayed in increasing observation ID, it does not necessarily mean successive points are observations performed immediately after each other.

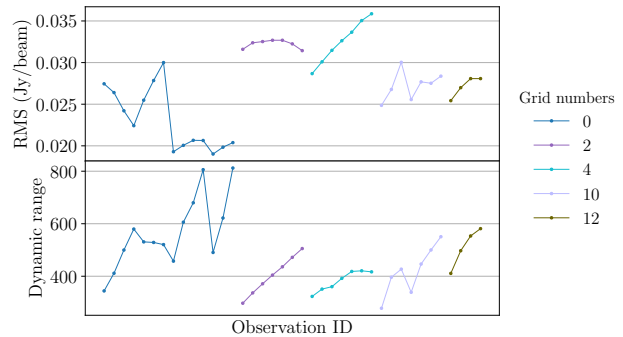


**Figure 2.** Image metrics for the EoR0 field grouped by pointing (represented by different colours) for observation IDs in ascending order. The top panel shows the Root Mean Square (RMS) metric. The bottom panel shows the Dynamic Range metric. The changing values between observations are due to sources moving in and out of the MWA beam.

#### 6.2 Amplitude solutions smoothness

The smoothness of both NS and EW polarisation amplitude calibration solutions for EoR0 can be found in Figure 3. Some fields exhibit clustering between lines of different observations IDs, this is especially prominent in the HERA LST 2.0 field in the NS amplitude smoothness found in Appendix 2. This clustering behaviour could be explained by different conditions at the time of observation or, simply, an insufficient amount of data to provide a robust representation of the field.

For a simplified version of the same data, a band plot of the same EoR0 data in Figure 3 is given in Figure 4, plotted in this figure are the median (red line), and the lower and upper quartiles (shaded region).

To showcase the smoothness metric, the NS amplitude solutions are given for observation 1201153128 at antennas 100 and 110 in Figure 5. From Figure 4 we can see that, generally, antenna 110 amplitude solutions are less smooth than the solutions of antenna 100. Indeed, this is the observed behaviour in Figure 5.

#### 6.3 Phase solutions metrics

The RMSE metrics for EoR0 are displayed in Figure 6. In this metric, a smaller number corresponds to a more linear phase solution. We once again observe similar clustering behaviour in some of these results. However, it appears that behaviour that is present in the amplitude calibration solutions does not necessarily translate to the phase metrics. The MAD behaves

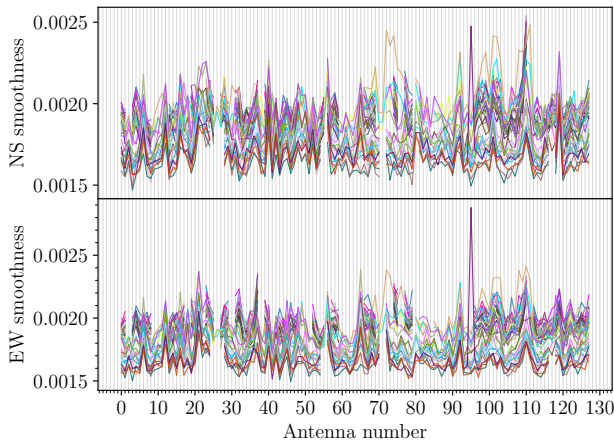


**Figure 3.** Smoothness of the NS (top) and EW (bottom) calibration amplitude solutions for EoR0 for each antenna. Each line represents a different observation ID. A smaller value represents smoother amplitude solutions.

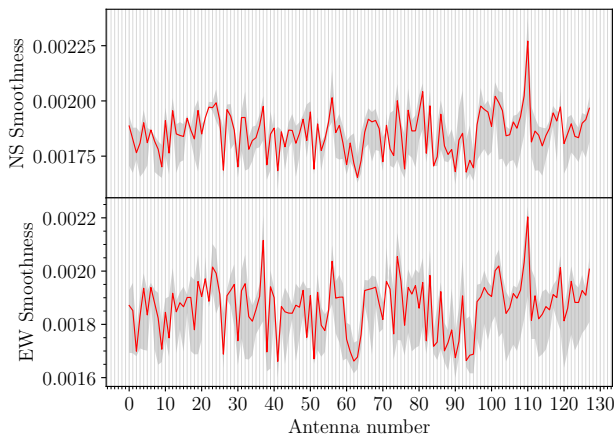


**Figure 4.** Band plot of the smoothness of the NS (top) and EW (bottom) amplitude calibration solutions for EoR0 for each antenna. The median per antenna is given in red, the upper and lower quartiles per antenna are given by the shaded region. A smaller value represents smoother amplitude solutions.

almost identically to the RMSE, hence, moving forward we focus on the RMSE metric.

Finally, the average Euclidean distance metrics for the EoR0 field are given in Figure 7. It is challenging to glean any information from the two similarity metrics, in particular the KS-metric seems to be the most random of all the metrics. For that reason, we will continue without KS-metric. However, in the average Euclidean distance metric some fields do exhibit clustering behaviour. For example, the EoR0 field appears to have two distinct groupings of average-distances, where one group is more similar than the other. Although it does exhibit more behaviour than the KS-metric, we opt to move without this metric going forward, as it is still difficult to obtain useful information.

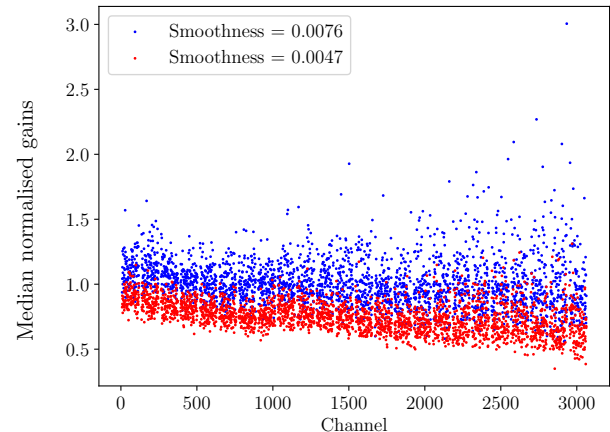


**Figure 5.** Calibration amplitude solutions for antenna 100 (red points) and antenna 110 (blue points) of observation 1201153128. A lower smoothness metric corresponds to visually smoother amplitudes. Indeed, we see that the antenna 100 (smoothness = 0.0047) is visually smoother than antenna 110 (smoothness = 0.0076).

#### 6.4 Smoothness and RMSE correlations

The NS smoothness and RMSE correlation plot for the EoR0 field can be found in Figure 8. In this figure, each colour and marker combination indicates an individual observation. Each point is described by the antenna's smoothness and RMSE metrics, and the opacity of the point relates to the antenna number. The more opaque points correspond to the long baseline tiles. In this figure, we can see for observations below RMSE=8, there exists a correlation between the smoothness and RMSE metric. As the amplitude solutions become less smooth (increasing smoothness metric) the RMSE metric also increases. This trend seems to flatten off for observations above RMSE=8 in the EoR0 field. Results for other fields, although not exactly the same shape, all show there is a positive correlation between these two metrics.

It is also worth noting in Figure 8 the clustering of observations with grid number 0 around RMSE values of 7, 12, and 14. A table of LSTs and start dates in UTC for observations with grid number 0 are given in Table 4. The cause of this clustering behaviour seem to stem from conditions at the time of observation and how close the observations are in terms of time.

#### 6.5 Theoretical gain uncertainties

The theoretical gain uncertainties for each field as a function of antenna number can be found in Figure 9. A combined histogram of the source brightness in each field is given in Figure 10 and the number of sources in each field along with the brightest source is given in Table 5. The three fields that produce the best gain uncertainties via the CRB matrix are SKAEOR15, EoR1, and HERA LST 5.2. These three fields show that having bright sources and a large number of points increase the gain precision.

The power spectra for each field, after propagating these



**Table 4.** Table of EoR0 observations with a grid number 0. The LST and start date in UTC are included for each observation. There are at least two large groups of observations which are close in time, while the others form smaller groups. These groupings could provide an explanation for the clustering of observations seen in Figure 8.

| Observation ID | LST    | Start date (UTC)    |
|----------------|--------|---------------------|
| 1286204984     | 361.98 | 2024-09-24T10:47:08 |
| 1286203784     | 356.97 | 2024-09-24T10:48:58 |
| 1286205584     | 364.49 | 2024-09-24T10:46:57 |
| 1286806936     | 356.98 | 2024-09-24T10:46:54 |
| 1286807536     | 359.49 | 2024-09-24T09:43:57 |
| 1194267224     | 358.92 | 2024-09-24T13:09:09 |
| 1194266984     | 357.91 | 2024-09-24T13:12:29 |
| 1286808736     | 364.50 | 2024-09-24T09:29:54 |
| 1194267464     | 359.92 | 2024-09-24T13:05:15 |
| 1286204384     | 359.48 | 2024-09-24T10:48:50 |
| 1194267704     | 0.92   | 2024-09-24T13:02:45 |
| 1194266744     | 356.91 | 2024-09-24T13:15:29 |
| 1194267944     | 1.92   | 2024-09-24T12:00:17 |
| 1194268184     | 2.93   | 2024-09-24T11:54:31 |

**Table 5.** Table of the number of sources within the field of view of the beam and the brightest source at 182 MHz during the Cramer-Rao Bound calculation, for each field. This table helps us reveal how the number of sources, and the brightest source result in the gain uncertainties we see in Figure 9.

| Field name   | Number of sources | Brightest source (Jy) |
|--------------|-------------------|-----------------------|
| EoR0         | 241               | 19.3                  |
| EoR1         | 233               | 32.4                  |
| HERA LST 2.0 | 170               | 16.2                  |
| HERA LST 5.2 | 220               | 50.0                  |
| SKAEOR5      | 219               | 23.3                  |
| SKAEOR6      | 240               | 23.3                  |
| SKAEOR14     | 170               | 8.6                   |
| SKAEOR15     | 274               | 14.2                  |

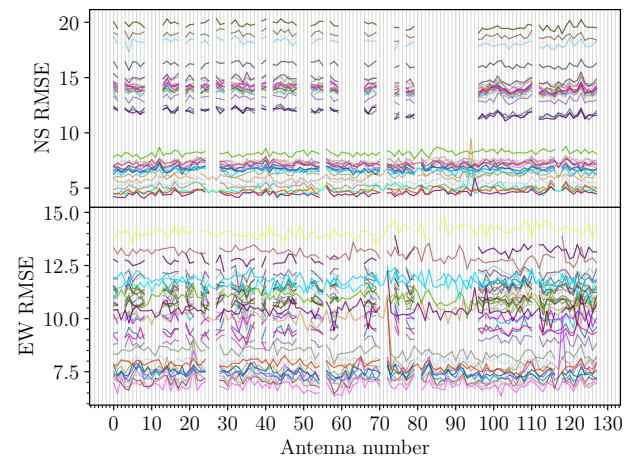


**Figure 6.** Root-Mean-Square-Error metric of both NS (top) and EW (bottom) calibration phase solutions for observations of the EoR0 field. Each line represents a different observation ID. A smaller value represents a more linear phase solution.

theoretical uncertainties into the visibilities, can be found in Figure 11. Interestingly, fields which have shown better theoretical calibration solutions previously do not have the best performing power spectra. This can be explained by considering Equation 13, the partial derivative coefficient is dependent on the brightness of the sources selected by the simulation. Hence, even if the gain uncertainties may be better for a particular field, they are imprinted upon the brightest sources in the field which may mean the power spectrum overall performs worse in comparison to other fields.

A 2D power spectrum for a pure 21 cm signal from a ‘faint galaxies’ model (de-projected from a 1D spherically averaged power spectrum, Mesinger, Greig, and Sobacchi 2016) is given in Figure 12. The theoretical power spectra of this work are at least an order of magnitude larger than the predicted signal.

## 7. Discussion

Having displayed the metrics and the theoretical analysis, we will attempt to select a few fields that may be ideal for EoR science. We will first begin by disentangling telescope-based effects from sky-based effects. Hence, our first criteria will be the number of observations available per field. This leaves us with four fields, these fields are: EoR0, HERA LST 5.2, SKAEOR5, and SKAEOR15. Within these fields, we inspect the average behaviour of the metrics, not the antenna to antenna or observation to observation behaviour, which should be uncorrelated. Figures for image metrics of the other metrics can be found in Appendix 1, amplitude smoothness in Appendix 2 and Appendix 3, phase RMSE in Appendix 4, and average Euclidean distance in Appendix 5.

Next, we narrow down the selection based on the performance of these four fields in the metrics. Table 6 displays how the fields compare relative to each other, where the comparison of metrics was a simple visual inspection. From this table, we can immediately exclude SKAEOR5 and SKAEOR15 from

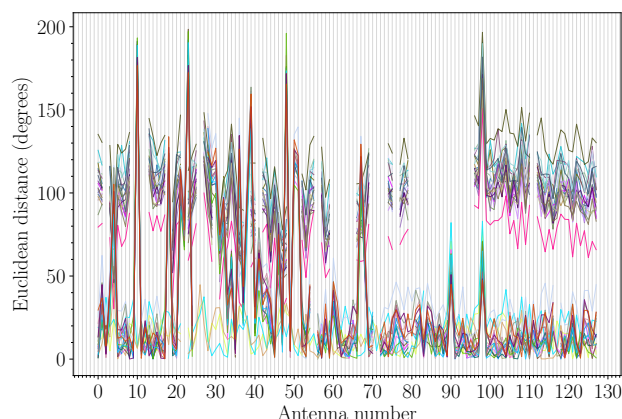


**Figure 7.** The average Euclidean distance metric between NS and EW calibration phase solutions for the EoR0 field. Each line represents a different observation ID. A lower value represents more similar phase solutions. In this field, there appears to be two groupings of distances where one group describes very similar phase solutions.

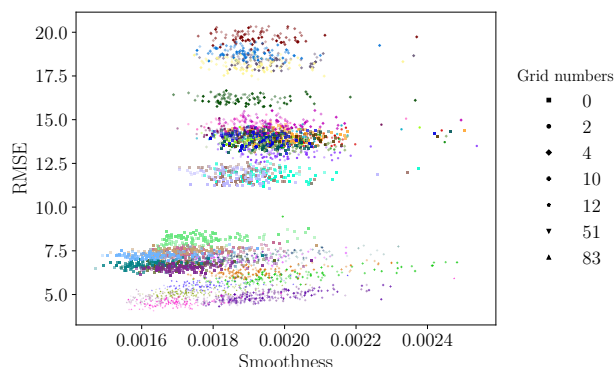


**Figure 8.** Plot displaying the correlation between the calibration amplitude smoothness metric and the NS calibration phase Root-Mean-Square-Error (RMSE) metric for observations of the EoR0 field. There is a positive correlation between the two metrics and seems to flatten off at higher RMSE values. Also seen is clustering of the observations with grid number 0, at RMSE values of 7, 12, and 14.

our selection, leaving only the EoR0 and HERA LST 5.2 fields.

Introducing the power spectra now will further narrow down the selection. To serve as a reminder, these power spectra showcase the impact of gain uncertainties due to the calibrators' positions within the beam. They also simulate a zenith pointing, hence simulations of these fields are not completely physical. Additionally, due to the sky model used in this study, some parts of the sky are better modelled than others.

With these factors in mind, from Figure 11 it is clear that the HERA LST 5.2 field is most affected by the gain uncertainties. The other three fields: EoR0, SKAEOR5, and SKAEOR15, display acceptable impacts from gain uncertainties. However, in reality, the SKAEOR5 field has a very northern declination, where the beam of the MWA starts to misbehave. Taking everything into account, the EoR0 field seems to be a safe field for observation.

We must also discuss the applicability of these metrics,

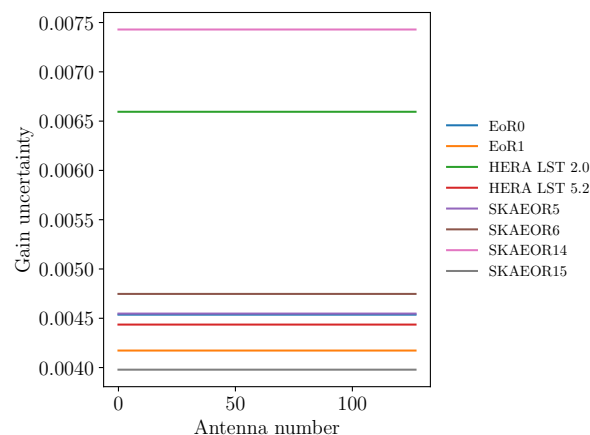


**Figure 9.** Theoretical gain uncertainties of various fields for 128 MWA antennas in the phase II configuration at 182 MHz, calculated with the procedure described in Section 5.3. Each field were treated as being zenith pointed. There are miniscule fluctuations between antennas for all fields.

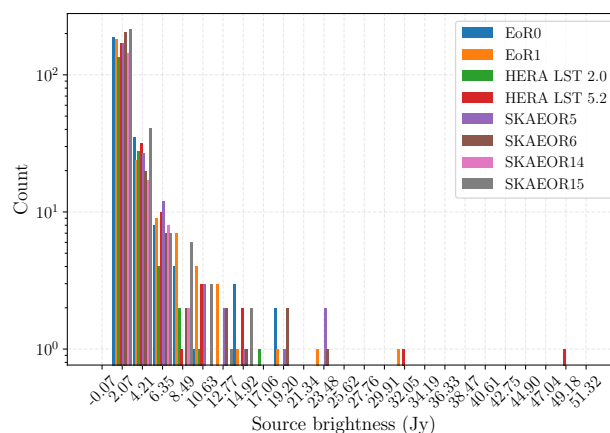


**Figure 10.** Combined histogram of source brightness for each field at 182 MHz during the Cramér-Rao Bounds calculation. The width of each bin is 2.14 Jy. This histogram, along with Table 5, help to investigate how the distribution of source brightness result in the gain uncertainties seen in Figure 9.

**Table 6.** Table of the four fields for consideration as an EoR observing field, and their relative performance to each other in the metrics used in this work. Performance was determined visually based on desired behaviours as described in Table 2. A check mark (✓) indicates the respective field(s) perform well in that metric, a tilde (∼) indicates reasonable performance, and a cross (×) indicates bad performance.

| Field        | Metrics   |          |                    |                    |               |               |
|--------------|-----------|----------|--------------------|--------------------|---------------|---------------|
|              | Image RMS | Image DR | XX Amp. Smoothness | YY Amp. Smoothness | XX Phase RMSE | YY Phase RMSE |
| EoR0         | ✓         | ✓        | ∼                  | ∼                  | ×             | ✓             |
| HERA LST 5.2 | ×         | ✓        | ✓                  | ✓                  | ✓             | ×             |
| SKAEOR5      | ∼         | ∼        | ×                  | ×                  | ×             | ×             |
| SKAEOR15     | ×         | ×        | ×                  | ×                  | ∼             | ✓             |

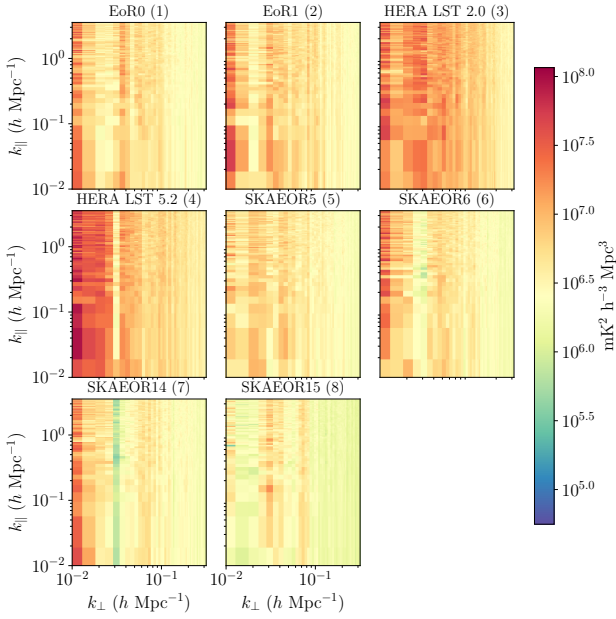


**Figure 11.** Resulting power spectra for each field after propagating theoretical uncertainties into visibilities. Each field was treated as if it were at zenith.

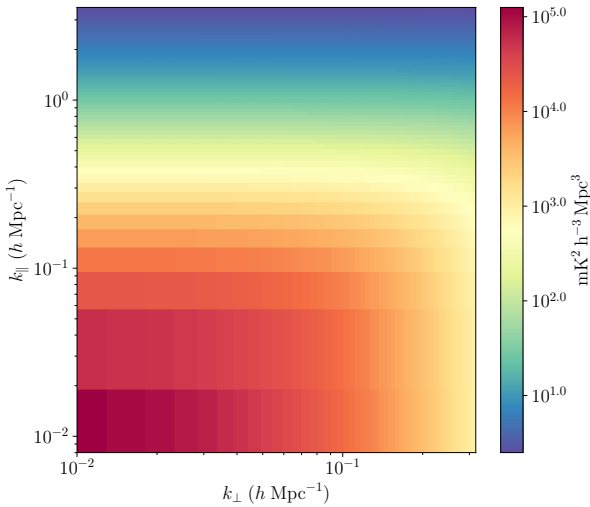


**Figure 12.** A 2D power spectrum of a pure 21 cm signal from a 'faint galaxies' simulation (Mesinger, Greig, and Sobacchi 2016) centred on  $z \sim 7$ .

which were calculated using archived MWA data, to the SKA-Low telescope. SKA-Low will have a much smaller field-of-view,  $\sim 2.5^\circ$  as opposed to  $\sim 21^\circ$  at 184.32 MHz, along with better sensitivity than the MWA. To compare the number of sources that would be detected by the MWA and SKA-Low, we can investigate the ratio of the integrated source counts,  $\frac{N_{\text{SKA}}}{N_{\text{MWA}}}$ . The integrated source count is given by

$$N(S > S_{\min}) = \frac{\alpha}{1 - \beta} \left( \frac{S_{\min}}{S_0} \right)^{1-\beta} \Omega, \quad (14)$$

where  $\alpha$  and  $\beta$  are fitting parameters that are intrinsic to the sky. The FOV,  $\Omega$ , can be approximated by  $\frac{\lambda}{D}$ , where  $D$  is the diameter of an MWA tile or SKA station.  $S_{\min}$  is the sensitivity of the MWA or SKA is given by Equation 10. In this section we express the sensitivity in the form

$$S_{\min} = \frac{\text{SEFD}}{\sqrt{\Delta\nu\Delta\tau\sqrt{N_b}}}, \quad (15)$$

where  $\Delta\nu$ ,  $\Delta\tau$ , and  $N_b$  are the bandwidth, integration times, and number of baselines respectively. The SEFD is calculated using

$$\text{SEFD} = \frac{2kT_{\text{sys}}}{A_e}, \quad (16)$$

where  $k$  is the Boltzmann constant, and  $A_e$  is the effective collecting area. The ratio of SKA integrated source counts to MWA integrated source counts is given by

$$\frac{N_{\text{SKA}}}{N_{\text{MWA}}} = \left( \frac{\text{SEFD}_{\text{SKA}} \sqrt{N_{b,\text{MWA}}}}{\text{SEFD}_{\text{MWA}} \sqrt{N_{b,\text{SKA}}}} \right)^{1-\beta} \frac{D_{\text{MWA}}}{D_{\text{SKA}}}, \quad (17)$$

where  $D_{\text{SKA}}$  and  $D_{\text{MWA}}$  are the diameters of an SKA station and MWA tile respectively (approximately 38m for the SKA and 4.4m for the MWA). For both SKA and MWA we assume  $T_{\text{sys}} \approx 200$  K at 150 MHz. The effective collecting area of the MWA at 150 MHz is  $A_{e,\text{MWA}} = 21.5 \text{ m}^2$ , for the SKA we will assume a single SKA station is 100% efficient resulting in  $A_{e,\text{SKA}} = 1134.11 \text{ m}^2$ . The system equivalent flux densities are then  $\text{SEFD}_{\text{MWA}} \approx 25000 \text{ Jy}$  and  $\text{SEFD}_{\text{SKA}} \approx 500 \text{ Jy}$ . In this calculation we use the source counts of Intema et al. 2011 to obtain  $\beta = 1.59$ . The number of unique baselines for SKA-Low and MWA are  $N_{b,\text{SKA}} = 131086$  and  $N_{b,\text{MWA}} = 8128$ .

With these values, Equation 17 is evaluated to approximately  $\frac{N_{\text{SKA}}}{N_{\text{MWA}}} \approx 0.5$ .

The SKA-Low will approximately detect half of what the MWA can detect, with the better sensitivity and smaller field of view. The effects of this will be difficult to discuss with certainty. But since we have shown a dependence on the number of sources and in particular the brightest sources, fields with bright sources near zenith in both the SKA and MWA field of view can be expected to behave similarly. Additionally, there is a dependence on the number of antennas in Equation 9. The combined effects of these dependencies is difficult to predict.

In the image metrics with SKA-Low, we can expect lower RMS and larger dynamic range (if a bright source is within the field of view) due to the increased sensitivity of SKA-Low. The calibration metrics are more challenging to estimate. We have seen with the HERA LST 5.2 simulation (which, in reality, is a zenith field) that the bright source contributes to a lower uncertainty, which is then reflected in the NS and EW amplitude smoothness metrics. Considering the correlation between amplitude smoothness and phase RMSE, we can further reason that the phase solutions should also be linear. Of course, this line of reasoning is only applied for the HERA LST 5.2 field and may not hold for other fields. Recently, work from LOFAR which uses a 6-hour observation of their target field containing 3C196 (Ceccotti *et al.* 2025), a very bright source near zenith, has seen lower systematics compared to the colder NCP field. This aligns with the behaviour we have explored in this work. We do not apply additional steps in the power spectrum estimation, hence, we cannot compare the power spectra of this work with those of the recent LOFAR work.

SKA-Low will also have the ability to form multiple beams and utilise sub-stations. It will also use digital beam formers which will allow for greater pointing precision. Further investigation into how these variables will affect EoR observations will be needed.

## 8. Conclusion

In this study we have investigated image metrics (RMS and dynamic range) and calibration metrics (amplitude smoothness, RMSE of the phase solutions, and average Euclidean distance between the phase solutions of different polarisations). We utilised archival MWA data in the phase II configuration centred on 184.32 MHz ( $z \sim 6.8$ ), with observations pointing towards fields used by the MWA collaboration (Lynch *et al.* 2021), HERA team (Abdurashidova *et al.* 2022), and fields previously chosen by other metrics (Zheng *et al.* 2020). These data were used as a proxy for future SKA-Low data. We found the most useful metrics to be the image RMS, dynamic range, amplitude smoothness, and phase RMSE.

In addition to the metrics, a theoretical method utilising the Crámer-Rao bound was used to calculate theoretical gain uncertainties. A standard error propagation of these uncertainties into the final power spectrum was also provided. From this we have seen that the brightest sources contribute the most to a lower gain uncertainty.

The combination of both metrics and theoretical power spectra helped to confirm that EoR0 is indeed a candidate for future EoR observations. In particular, the field's performance in the both image metrics, and its impacts on the final power spectrum — while also being a real pointing used by the MWA — has led us to this conclusion. However, this shouldn't dissuade the investigation of the other fields. The HERA LST 5.2 field was shown to perform well in the smoothness metric, which aligns with behaviour in recent work from LOFAR (Ceccotti *et al.* 2025). Additionally, the HERA LST 5.2 field has the largest dynamic ranges (but also large RMS) out of the fields discussed. The SKAEOR5 field, which contains the second-largest number of observations has a slowly varying image RMS second to the EoR0 RMS. Clearly, these fields are still worth investigating.

## Acknowledgement

This research was partly supported by the Australian Research Council Centre of Excellence for All Sky Astrophysics in 3 Dimensions (ASTRO 3D), through project number CE170100013. The International Centre for Radio Astronomy Research (ICRAR) is a Joint Venture of Curtin University and The University of Western Australia, funded by the Western Australian State government. This scientific work uses data obtained from *Inyarri-manha Ilgari Bundara* / the Murchison Radio-astronomy Observatory. We acknowledge the Wajarri Yamaji People as the Traditional Owners and native title holders of the Observatory site. Establishment of CSIRO's Murchison Radio-astronomy Observatory is an initiative of the Australian Government, with support from the Government of Western Australia and the Science and Industry Endowment Fund. Support for the operation of the MWA is provided by the Australian Government (NCRIS), under a contract to Curtin University administered by Astronomy Australia Limited. This work was supported by resources provided by the Pawsey Supercomputing Research Centre with funding from the Australian Government and the Government of Western Australia.



## References

- Abdurashidova, Zara, James E. Aguirre, Paul Alexander, Zaki S. Ali, Yanga Balfour, Adam P. Beardsley, Gianni Bernardi, et al. 2022. First Results from HERA Phase I: Upper Limits on the Epoch of Reionization 21 cm Power Spectrum. *The Astrophysical Journal* 925, no. 2 (February): 221. <https://doi.org/10.3847/1538-4357/ac1c78>. arXiv: 2108.02263 [astro-ph.CO].
- Acharya, Anshuman, Florent Mertens, Benedetta Ciardi, Raghunath Ghara, Léon V E Koopmans, and Saleem Zaroubi. 2024. Revised lofar upper limits on the 21-cm signal power spectrum at  $z \approx 9.1$  using machine learning and gaussian process regression. *Monthly Notices of the Royal Astronomical Society: Letters* 534, no. 1 (August): L30–L34. ISSN: 1745-3933. <https://doi.org/10.1093/mnras/lsae078>.
- Asad, K. M. B., L. V. E. Koopmans, V. Jelić, V. N. Pandey, A. Ghosh, F. B. Abdalla, G. Bernardi, et al. 2015. Polarization leakage in epoch of reionization windows – I. Low Frequency Array observations of the 3C196 field. *Monthly Notices of the Royal Astronomical Society* 451, no. 4 (August): 3709–3727. <https://doi.org/10.1093/mnras/stv1107>. arXiv: 1503.01644 [astro-ph.CO].
- Barry, N., B. Hazelton, I. Sullivan, M. F. Morales, and J. C. Pober. 2016. Calibration requirements for detecting the 21 cm epoch of reionization power spectrum and implications for the ska. *Monthly Notices of the Royal Astronomical Society* 461, no. 3 (June): 3135–3144. ISSN: 1365-2966. <https://doi.org/10.1093/mnras/stw1380>.
- Barry, N., M. Wilensky, C. M. Trott, B. Pindor, A. P. Beardsley, B. J. Hazelton, I. S. Sullivan, et al. 2019. Improving the epoch of reionization power spectrum results from murchison widefield array season 1 observations. *The Astrophysical Journal* 884, no. 1 (October): 1. ISSN: 1538-4357. <https://doi.org/10.3847/1538-4357/ab40a8>.
- Bowman, Judd D., and Alan E. E. Rogers. 2010. A lower limit of  $\Delta z > 0.06$  for the duration of the reionization epoch. *Nature* 468, no. 7325 (December): 796–798. ISSN: 1476-4687. <https://doi.org/10.1038/nature09601>.
- Brackenhoff, S A, A R Offringa, M Mevius, L V E Koopmans, J K Chege, E Ceccotti, C Höfer, et al. 2025. Robust direction-dependent gain-calibration of beam-modelling errors far from the target field. *Monthly Notices of the Royal Astronomical Society* 541, no. 4 (July): 3993–4010. ISSN: 1365-2966. <https://doi.org/10.1093/mnras/staf1206>.
- Byrne, Ruby, Miguel F. Morales, Bryna Hazelton, Wenyang Li, Nichole Barry, Adam P. Beardsley, Ronniy Joseph, Jonathan Pober, Ian Sullivan, and Cathryn Trott. 2019. Fundamental limitations on the calibration of redundant 21 cm cosmology instruments and implications for hera and the ska. *The Astrophysical Journal* 875, no. 1 (April): 70. ISSN: 1538-4357. <https://doi.org/10.3847/1538-4357/ab107d>.
- Ceccotti, E., A. R. Offringa, F. G. Mertens, L. V. E. Koopmans, S. Munshi, J. K. Chege, A. Acharya, et al. 2025. First upper limits on the 21-cm signal power spectrum of neutral hydrogen at  $z = 9.16$  from the lofar 3c196 field. <https://doi.org/10.48550/ARXIV.2504.18534>.
- Chapman, Emma, and Vibor Jelić. 2019. Foregrounds and their mitigation. In *The cosmic 21-cm revolution*, 6–1–6–29. IOP Publishing, December. ISBN: 9780750322348. <https://doi.org/10.1088/2514-3433/ab4a73ch6>.
- Chokshi, A, N Barry, J L B Line, C H Jordan, B Pindor, and R L Webster. 2024. The necessity of individually validated beam models for an interferometric epoch of reionization detection. *Monthly Notices of the Royal Astronomical Society* 534, no. 3 (October): 2475–2484. ISSN: 1365-2966. <https://doi.org/10.1093/mnras/stae2264>.
- Cook, J. H., C. M. Trott, and J. L. B. Line. 2022. Investigating the contribution of extended radio sources to the Epoch of Reionization power spectrum. *Monthly Notices of the Royal Astronomical Society* 514, no. 1 (July): 790–805. <https://doi.org/10.1093/mnras/stac1330>. arXiv: 2205.04644 [astro-ph.CO].
- DeBoer, David R., Aaron R. Parsons, James E. Aguirre, Paul Alexander, Zaki S. Ali, Adam P. Beardsley, Gianni Bernardi, et al. 2017. Hydrogen epoch of reionization array (hera). *Publications of the Astronomical Society of the Pacific* 129, no. 974 (March): 045001. ISSN: 1538-3873. <https://doi.org/10.1088/1538-3873/129/974/045001>.
- Eastwood, Michael W., Marin M. Anderson, Ryan M. Monroe, Gregg Hal-linan, Morgan Catha, Jayce Dowell, Hugh Garsden, et al. 2019. The 21 cm power spectrum from the cosmic dawn: first results from the ovro-lwa. *The Astronomical Journal* 158, no. 2 (July): 84. ISSN: 1538-3881. <https://doi.org/10.3847/1538-3881/ab2629>.
- Ellingson, Steven W., Tracy E. Clarke, Aaron Cohen, Joseph Craig, Namir E. Kassim, Ylva Pihlstrom, Lee J Rickard, and Gregory B. Taylor. 2009. The long wavelength array. *Proceedings of the IEEE* 97, no. 8 (August): 1421–1430. ISSN: 1558-2256. <https://doi.org/10.1109/jproc.2009.2015683>.
- Ewall-Wice, Aaron, Joshua S. Dillon, Adrian Liu, and Jacqueline Hewitt. 2017. The impact of modelling errors on interferometer calibration for 21 cm power spectra. *Monthly Notices of the Royal Astronomical Society* 470, no. 2 (May): 1849–1870. ISSN: 1365-2966. <https://doi.org/10.1093/mnras/stx1221>.
- Furlanetto, Steven R., S. Peng Oh, and Frank H. Briggs. 2006. Cosmology at low frequencies: the 21cm transition and the high-redshift universe. *Physics Reports* 433, no. 4–6 (October): 181–301. ISSN: 0370-1573. <https://doi.org/10.1016/j.physrep.2006.08.002>.
- Haarlem, M. P. van, M. W. Wise, A. W. Gunst, G. Heald, J. P. McKean, J. W. T. Hessels, A. G. de Bruyn, et al. 2013. Lofar: the low-frequency array. *Astronomy & Astrophysics* 556 (July): A2. ISSN: 1432-0746. <https://doi.org/10.1051/0004-6361/201220873>.
- Haslam, C. G. T., C. J. Salter, H. Stoffel, and W. E. Wilson. 1982. A 408-MHZ All-Sky Continuum Survey. II. The Atlas of Contour Maps. *Astronomy and Astrophysics, Supplement* 47 (January): 1.
- HERA Collaboration, Zara Abdurashidova, Tyrone Adams, James E. Aguirre, Paul Alexander, Zaki S. Ali, Rushelle Baartman, et al. 2023. Improved Constraints on the 21 cm EoR Power Spectrum and the X-Ray Heating of the IGM with HERA Phase I Observations. *The Astrophysical Journal* 945, no. 2 (March): 124. <https://doi.org/10.3847/1538-4357/acaf50>. arXiv: 2210.04912 [astro-ph.CO].
- Högbom, J. A. 1974. Aperture synthesis with a non-regular distribution of interferometer baselines. *Astronomy and Astrophysics Supplement* 15 (June): 417.
- Hurley-Walker, N, J R Callingham, P J Hancock, T M O Franzen, L Hindson, A D Kapińska, J Morgan, et al. 2016. Galactic and extragalactic all-sky murchison widefield array (gleam) survey – i. a low-frequency extragalactic catalogue. *Monthly Notices of the Royal Astronomical Society* 464, no. 1 (September): 1146–1167. ISSN: 1365-2966. <https://doi.org/10.1093/mnras/stw2337>.
- Ikeda, Shiro, Takeshi Nakazato, Takashi Tsukagoshi, Tsutomu T Takeuchi, and Masayuki Yamaguchi. 2025. Solving self-calibration of alma data with an optimization method. *Publications of the Astronomical Society of Japan* 77, no. 2 (February): 260–276. ISSN: 2053-051X. <https://doi.org/10.1093/pasj/psae114>.
- Intema, H. T., R. J. van Weeren, H. J. A. Röttgering, and D. V. Lal. 2011. Deep low-frequency radio observations of the noao boötes field: i. data reduction and catalog construction. *Astronomy & Astrophysics* 535 (October): A38. ISSN: 1432-0746. <https://doi.org/10.1051/0004-6361/201014253>.
- Jacobs, Daniel C., B. J. Hazelton, C. M. Trott, Joshua S. Dillon, B. Pindor, I. S. Sullivan, J. C. Pober, et al. 2016. The murchison widefield array 21 cm power spectrum analysis methodology. *The Astrophysical Journal* 825, no. 2 (July): 114. ISSN: 1538-4357. <https://doi.org/10.3847/0004-637x/825/2/114>.

- Jordan, Christopher, Dev Null, Cathryn Trott, Jack Line, Kariuki Chege, Christene Lynch, Chuneeta Nunhokee, Greg Slep, and Randall Wayth. 2025. *Mwa\_hyperdrive: next generation calibration software for the murchison widefield array radio telescope*. In *Proceedings of the 7th urisi asia-pacific radioscience conference – ap-rasc 2025*. URSI AP-RASC 2025. URSI – International Union of Radio Science. <https://doi.org/10.46620/ursiapasc25/lscn1310>.
- Kay, S. M. 1993. *Fundamentals of statistical signal processing: estimation theory*. Prentice-Hall.
- Koopmans, Leon, J Pritchard, G Mellema, J Aguirre, K Ahn, R Barkana, I van Bommel, et al. 2015. The cosmic dawn and epoch of reionisation with ska. In *Proceedings of advancing astrophysics with the square kilometre array — pos(aaska14)*. AASKA14. Sissa Medialab, May. <https://doi.org/10.22323/1.215.0001>.
- Lessard, Charles S. 2006. Window functions and spectral leakage. In *Signal processing of random physiological signals*, 175–193. Springer International Publishing. ISBN: 9783031016103. [https://doi.org/10.1007/978-3-031-01610-3\\_16](https://doi.org/10.1007/978-3-031-01610-3_16).
- Line, J. L. B., D. A. Mitchell, B. Pindor, J. L. Riding, B. McKinley, R. L. Webster, C. M. Trott, N. Hurley-Walker, and A. R. Offringa. 2020. Modelling and peeling extended sources with shapelets: a fornax a case study. *Publications of the Astronomical Society of Australia* 37. ISSN: 1448-6083. <https://doi.org/10.1017/pasa.2020.18>.
- Lynch, C. R., T. J. Galvin, J. L. B. Line, C. H. Jordan, C. M. Trott, J. K. Chege, B. McKinley, M. Johnston-Hollitt, and S. J. Tingay. 2021. The mwa long baseline epoch of reionisation survey—i. improved source catalogue for the eor 0 field. *Publications of the Astronomical Society of Australia* 38. ISSN: 1448-6083. <https://doi.org/10.1017/pasa.2021.50>.
- Mertens, F. G., M. Mevius, L. V. E. Koopmans, A. R. Offringa, G. Mellema, S. Zaroubi, M. A. Brentjens, et al. 2020. Improved upper limits on the 21 cm signal power spectrum of neutral hydrogen at  $z \approx 9.1$  from LOFAR. *Monthly Notices of the Royal Astronomical Society* 493, no. 2 (April): 1662–1685. <https://doi.org/10.1093/mnras/staa327>. arXiv: 2002.07196 [astro-ph.CO].
- Mertens, F. G., M. Mevius, L. V. E. Koopmans, A. R. Offringa, S. Zaroubi, A. Acharya, S. A. Brackenhoff, et al. 2025. Deeper multi-redshift upper limits on the epoch of reionisation 21 cm signal power spectrum from LOFAR between  $z = 8.3$  and  $z = 10.1$ . *A&A* 698 (June): A186. <https://doi.org/10.1051/0004-6361/202554158>. arXiv: 2503.05576 [astro-ph.CO].
- Mesinger, Andrei, Bradley Greig, and Emanuele Sobacchi. 2016. The evolution of 21 cm structure (eos): public, large-scale simulations of cosmic dawn and reionization. *Monthly Notices of the Royal Astronomical Society* 459, no. 3 (April): 2342–2353. ISSN: 1365-2966. <https://doi.org/10.1093/mnras/stw831>.
- Mitchell, D.A., L.J. Greenhill, R.B. Wayth, R.J. Sault, C.J. Lonsdale, R.J. Cappallo, M.F. Morales, and S.M. Ord. 2008. Real-time calibration of the murchison widefield array. *IEEE Journal of Selected Topics in Signal Processing* 2, no. 5 (October): 707–717. ISSN: 1941-0484. <https://doi.org/10.1109/jstsp.2008.2005327>.
- Munshi, S., F. G. Mertens, J. K. Chege, L. V. E. Koopmans, A. R. Offringa, B. Semelin, R. Barkana, et al. 2025. Improved upper limits on the 21-cm signal power spectrum at  $z = 17.0$  and  $z = 20.3$  from an optimal field observed with nenufar. <https://doi.org/10.48550/ARXIV.2507.10533>.
- Munshi, S., F. G. Mertens, L. V. E. Koopmans, A. R. Offringa, B. Semelin, D. Aubert, R. Barkana, et al. 2024. First upper limits on the 21 cm signal power spectrum from cosmic dawn from one night of observations with nenufar. *Astronomy & Astrophysics* 681 (January): A62. ISSN: 1432-0746. <https://doi.org/10.1051/0004-6361/202348329>.
- Nunhokee, C. D., D. Null, C. M. Trott, N. Barry, Y. Qin, R. B. Wayth, J. L. B. Line, et al. 2025. Limits on the 21 cm Power Spectrum at  $z = 6.5$ – $7.0$  from Murchison Widefield Array Observations. *The Astrophysical Journal* 989, no. 1 (August): 57. <https://doi.org/10.3847/1538-4357/adda45>. arXiv: 2505.09097 [astro-ph.CO].
- Nunhokee, C. D., Dev Null, Cathryn Trott, Christopher Jordan, Jack Laurence Bramble Line, Randall Bruce Wayth, and Nichole Barry. 2024. Strategy for mitigation of systematics for EoR experiments with the Murchison Widefield Array. *Publications of the Astronomical Society of Australia* 41 (December): e095. <https://doi.org/10.1017/pasa.2024.87>. arXiv: 2409.03232 [astro-ph.CO].
- Nunhokee, C. D., Aaron R. Parsons, Nicholas S. Kern, Bojan Nikolic, Jonathan C. Pober, Gianni Bernardi, Chris L. Carilli, et al. 2020. Measuring HERA's Primary Beam in Situ: Methodology and First Results. *The Astrophysical Journal* 897, no. 1 (July): 5. <https://doi.org/10.3847/1538-4357/ab9634>. arXiv: 2005.12174 [astro-ph.IM].
- Offringa, A. R., B. McKinley, N. Hurley-Walker, F. H. Briggs, R. B. Wayth, D. L. Kaplan, M. E. Bell, et al. 2014. Wsclean: an implementation of a fast, generic wide-field imager for radio astronomy. *Monthly Notices of the Royal Astronomical Society* 444, no. 1 (August): 606–619. ISSN: 1365-2966. <https://doi.org/10.1093/mnras/stu1368>.
- Offringa, A. R., R. B. Wayth, N. Hurley-Walker, D. L. Kaplan, N. Barry, A. P. Beardsley, M. E. Bell, et al. 2015. The low-frequency environment of the murchison widefield array: radio-frequency interference analysis and mitigation. *Publications of the Astronomical Society of Australia* 32. ISSN: 1448-6083. <https://doi.org/10.1017/pasa.2015.7>.
- Paciga, Gregory, Tzu-Ching Chang, Yashwant Gupta, Rajaram Nityanada, Julia Odegova, Ue-Li Pen, Jeffrey B. Peterson, Jayanta Roy, and Kris Sigurdson. 2011. The gmrt epoch of reionization experiment: a new upper limit on the neutral hydrogen power spectrum at  $z \approx 8.6$ : the gmrt-eor experiment: h i power spectrum. *Monthly Notices of the Royal Astronomical Society* 413, no. 2 (March): 1174–1183. ISSN: 0035-8711. <https://doi.org/10.1111/j.1365-2966.2011.18208.x>.
- Pritchard, Jonathan R, and Abraham Loeb. 2012. 21 cm cosmology in the 21st century. *Reports on Progress in Physics* 75, no. 8 (July): 086901. ISSN: 1361-6633. <https://doi.org/10.1088/0034-4885/75/8/086901>.
- Procopio, P., R. B. Wayth, J. Line, C. M. Trott, H. T. Intema, D. A. Mitchell, B. Pindor, et al. 2017. A high-resolution foreground model for the mwa eor1 field: model and implications for eor power spectrum analysis. *Publications of the Astronomical Society of Australia* 34 (August). ISSN: 1448-6083. <https://doi.org/10.1017/pasa.2017.26>.
- Rahimi, M, B Pindor, J L B Line, N Barry, C M Trott, R L Webster, C H Jordan, et al. 2021. Epoch of reionization power spectrum limits from murchison widefield array data targeted at eor1 field. *Monthly Notices of the Royal Astronomical Society* 508, no. 4 (October): 5954–5971. ISSN: 1365-2966. <https://doi.org/10.1093/mnras/stab2918>.
- Sokolowski, M., T. Colegate, A. T. Sutinjo, D. Ung, R. Wayth, N. Hurley-Walker, E. Lenc, et al. 2017. Calibration and stokes imaging with full embedded element primary beam model for the murchison widefield array. *Publications of the Astronomical Society of Australia* 34. ISSN: 1448-6083. <https://doi.org/10.1017/pasa.2017.54>.
- Storey, J. W. V., M. C. B. Ashley, M. Naray, and J. P. Lloyd. 1994. 21 cm line of atomic hydrogen. *American Journal of Physics* 62, no. 12 (December): 1077–1081. ISSN: 1943-2909. <https://doi.org/10.1119/1.17664>.
- Swarup, G., S. Ananthakrishnan, V. K. Kapahi, A. P. Rao, C. R. Subrahmanya, and V. K. Kulkarni. 1991. The giant metre-wave radio telescope. *Current Science* 60 (2): 95–105. ISSN: 00113891, accessed March 23, 2025. <http://www.jstor.org/stable/24094934>.
- Tingay, S. J., R. Goeke, J. D. Bowman, D. Emrich, S. M. Ord, D. A. Mitchell, M. F. Morales, et al. 2013. The murchison widefield array: the square kilometre array precursor at low radio frequencies. *Publications of the Astronomical Society of Australia* 30. ISSN: 1448-6083. <https://doi.org/10.1017/pasa.2012.007>.
- Trott, Cathryn M., C. H. Jordan, S. Midgley, N. Barry, B. Greig, B. Pindor, J. H. Cook, et al. 2020. Deep multiredshift limits on Epoch of Reionization 21 cm power spectra from four seasons of Murchison Widefield Array observations. *Monthly Notices of the Royal Astronomical Society* 493, no. 4 (April): 4711–4727. <https://doi.org/10.1093/mnras/staa414>. arXiv: 2002.02575 [astro-ph.CO].

- Trott, Cathryn M., Randall B. Wayth, Jean-Pierre R. Macquart, and Steven J. Tingay. 2011. Source Detection in Interferometric Visibility Data. I. Fundamental Estimation Limits. *The Astrophysical Journal* 731, no. 2 (April): 81. <https://doi.org/10.1088/0004-637X/731/2/81>. arXiv: 1102.3746 [astro-ph.IM].
- Virtanen, Pauli, Ralf Gommers, Travis E. Oliphant, Matt Haberland, Tyler Reddy, David Cournapeau, Evgeni Burovski, et al. 2020. Scipy 1.0: fundamental algorithms for scientific computing in python. *Nature Methods* 17, no. 3 (February): 261–272. ISSN: 1548-7105. <https://doi.org/10.1038/s41592-019-0686-2>.
- Warnick, Karl F., Rob Maaskant, Marianna V. Ivashina, David B. Davidson, and Brian D. Jeffs. 2018. *Phased arrays for radio astronomy, remote sensing, and satellite communications*. Cambridge University Press, July. ISBN: 9781108539258. <https://doi.org/10.1017/9781108539258>.
- Wayth, R. B., E. Lenc, M. E. Bell, J. R. Callingham, K. S. Dwarakanath, T. M. O. Franzen, B. -Q. For, et al. 2015. GLEAM: The GaLactic and Extragalactic All-Sky MWA Survey. *Publications of the Astronomical Society of Australia* 32 (June): e025. <https://doi.org/10.1017/pasa.2015.26>. arXiv: 1505.06041 [astro-ph.IM].
- Wayth, R. B., Steven J. Tingay, Cathryn M. Trott, David Emrich, Melanie Johnston-Hollitt, Ben McKinley, B. M. Gaensler, et al. 2018. The Phase II Murchison Widefield Array: Design overview. *Publications of the Astronomical Society of Australia* 35 (November): e033. <https://doi.org/10.1017/pasa.2018.37>. arXiv: 1809.06466 [astro-ph.IM].
- Yatawatta, S., A. G. de Bruyn, M. A. Brentjens, P. Labropoulos, V. N. Pandey, S. Kazemi, S. Zaroubi, et al. 2013. Initial deep lofar observations of epoch of reionization windows: i. the north celestial pole. *Astronomy & Astrophysics* 550 (February): A136. ISSN: 1432-0746. <https://doi.org/10.1051/0004-6361/201220874>.
- Yatawatta, Sarod. 2015. Distributed radio interferometric calibration. *Monthly Notices of the Royal Astronomical Society* 449, no. 4 (April): 4506–4514. ISSN: 1365-2966. <https://doi.org/10.1093/mnras/stv596>.
- Zarka, P., M. Tagger, L. Denis, J. N. Girard, A. Kononenko, M. Atemkeng, M. Arnaud, et al. 2015. Nenufar: instrument description and science case. In *2015 international conference on antenna theory and techniques (icatt)*, 1–6. IEEE, April. <https://doi.org/10.1109/icatt.2015.7136773>.
- Zheng, Qian, Xiang-Ping Wu, Quan Guo, Melanie Johnston-Hollitt, Huanyuan Shan, Stefan W. Duchesne, and Weitian Li. 2020. Pre-selection of the candidate fields for deep imaging of the epoch of reionization with ska1-low. *Monthly Notices of the Royal Astronomical Society* 499, no. 3 (October): 3434–3444. ISSN: 1365-2966. <https://doi.org/10.1093/mnras/staa3011>.

## Appendix 1. Image metrics

This appendix contains figures for the image RMS and dynamic range metrics for the HERA LST 5.2, SKAEOR5, and SKAEOR15 fields for comparison. A low RMS and large dynamic range are ideal behaviours for these metrics. Interestingly, the SKAEOR5 field (Figure 14) displays slowly varying RMS over a large number of observations.

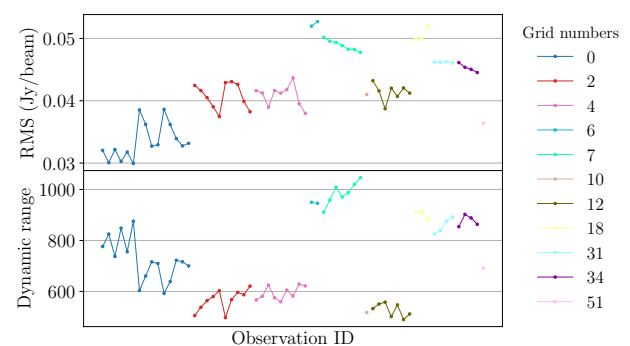


**Figure 13.** The RMS of the HERA field at LST 5.2 is shown in the top plot, the dynamic range is shown in the bottom plot. Different colours correspond to different grid numbers in the field. Each point within each pointing corresponds to an observation ID, with observation IDs increasing within a pointing.

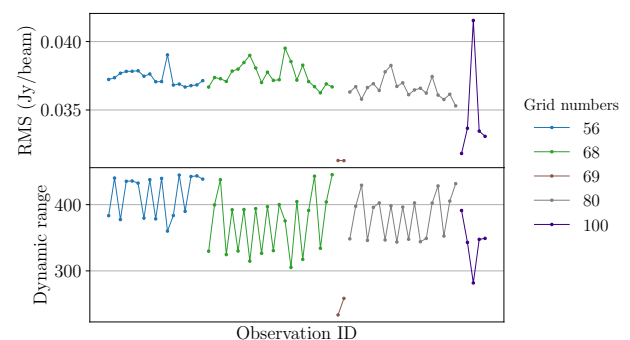


**Figure 14.** The RMS of the SKAEOR5 field is shown in the top plot, the dynamic range is shown in the bottom plot. Different colours correspond to different grid numbers in the field. Each point within each pointing corresponds to an observation ID, with observation IDs increasing within a pointing.

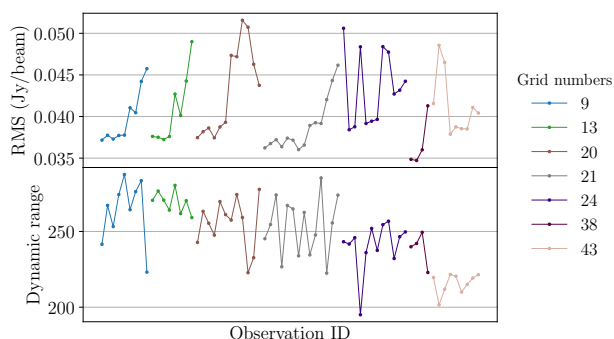


**Figure 15.** The RMS of the SKAER15 field is shown in the top plot, the dynamic range is shown in the bottom plot. Different colours correspond to different grid numbers in the field. Each point within each pointing corresponds to an observation ID, with observation IDs increasing within a pointing.

## Appendix 2. Amplitude smoothness

This appendix contains figures for the calibration amplitude smoothness metric for the HERA LST 5.2, SKAER5, and SKAER15 fields for comparison. Alongside these figures, the HERA LST 2.0 field is presented to show the clustering behaviour of observations, likely arising from a lack of observations. This metric indicates smoother amplitude solutions when it occupies values closer to 0.

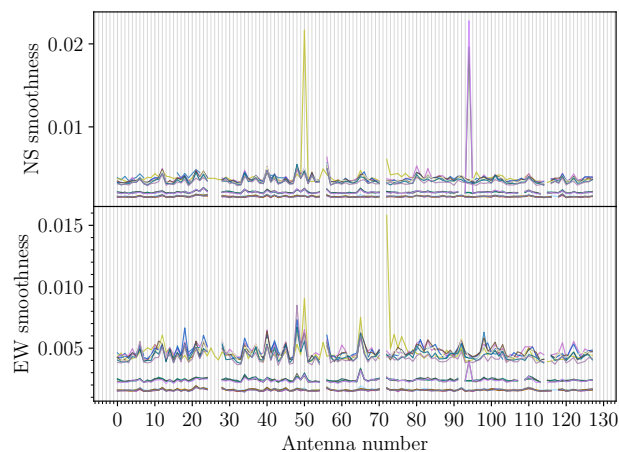


**Figure 16.** Smoothness of the NS (top) and EW (bottom) amplitude calibration solutions for HERA LST 2.0 for each antenna. Different colours represent a different observation ID. A lower value is ideal and indicates smoother calibration amplitude solutions. The clear grouping of observations likely arise from a lack of data for this field.

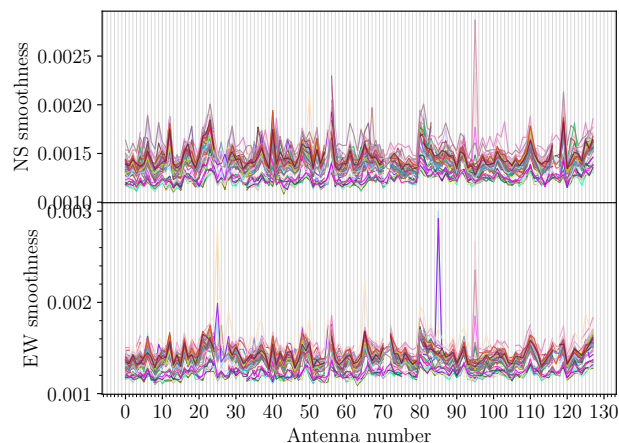


**Figure 17.** Smoothness of the NS (top) and EW (bottom) amplitude calibration solutions for HERA LST 5.2 for each antenna. Different colours represent a different observation ID. A lower value is ideal and indicates smoother calibration amplitude solutions



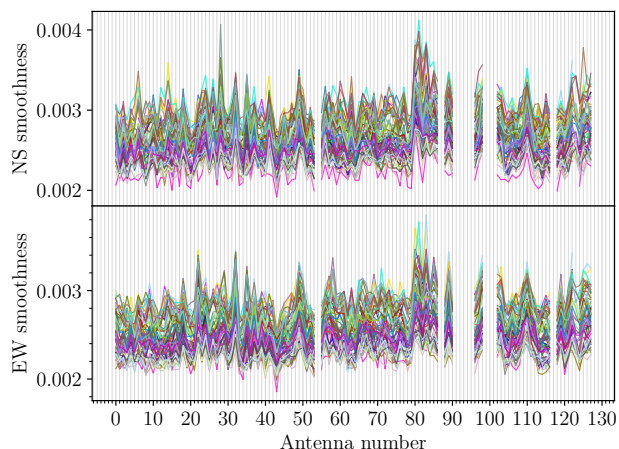


**Figure 18.** Smoothness of the NS (top) and EW (bottom) amplitude calibration solutions for SKAOR5 for each antenna. Different colours represent a different observation ID. A lower value is ideal and indicates smoother calibration amplitude solutions.

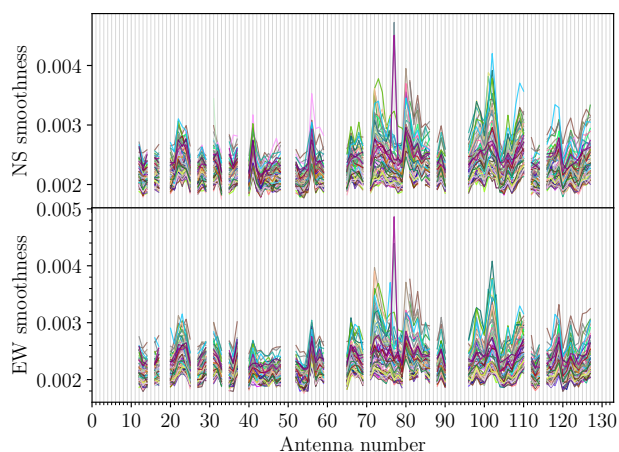


**Figure 19.** Smoothness of the NS (top) and EW (bottom) amplitude calibration solutions for SKAOR15 for each antenna. Different colours represent a different observation ID. A lower value is ideal and indicates smoother calibration amplitude solutions.

### Appendix 3. Smoothness band plots

This appendix contains figures for the calibration amplitude smoothness metric for the HERA LST 5.2, SKAOR5, and SKAOR15 fields in the form of band plots for comparison. The same data used to generate the figures in Appendix Appendix 2 are used here. The plotted red line in these figures is the median value at each antenna. The shaded region represents the interquartile range of the data.

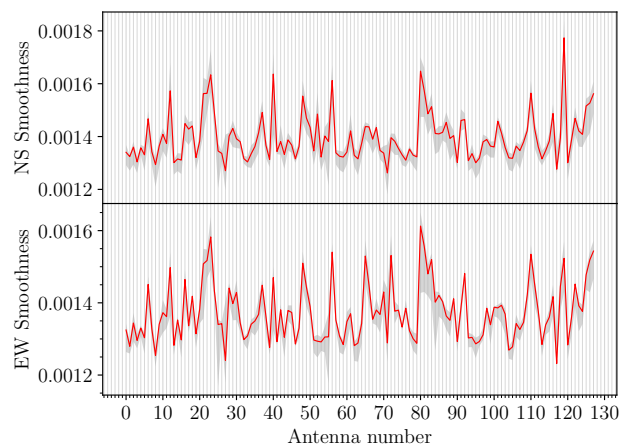


**Figure 20.** Smoothness of the NS (top) and EW (bottom) amplitude calibration solutions for HERA LST 5.2 for each antenna. The red line represents the median value at each antenna, while the shaded region represents the interquartile range of the data. A lower value is ideal and indicates smoother calibration amplitude solutions.

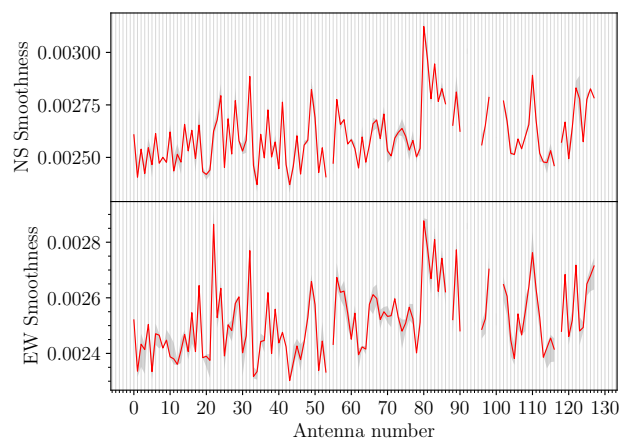


**Figure 21.** Smoothness of the NS (top) and EW (bottom) amplitude calibration solutions for SKAOR5 for each antenna. The red line represents the median value at each antenna, while the shaded region represents the interquartile range of the data. A lower value is ideal and indicates smoother calibration amplitude solutions.

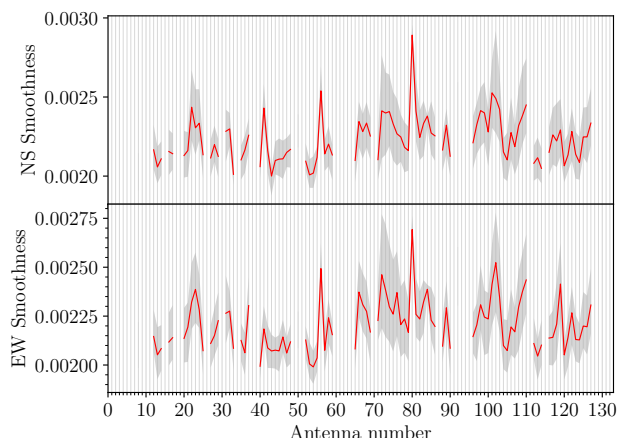


**Figure 22.** Smoothness of the NS (top) and EW (bottom) amplitude calibration solutions for SKAEOR15 for each antenna. The red line represents the median value at each antenna, while the shaded region represents the interquartile range of the data. A lower value is ideal and indicates smoother calibration amplitude solutions.

#### Appendix 4. RMSE metrics

This appendix contains figures for the calibration phase RMSE metric for the HERA LST 5.2, SKAEOR5, and SKAEOR15 fields for comparison. This metric aims to measure the linearity of the phase solutions, where more linear phase solutions correspond to a lower RMSE metric.

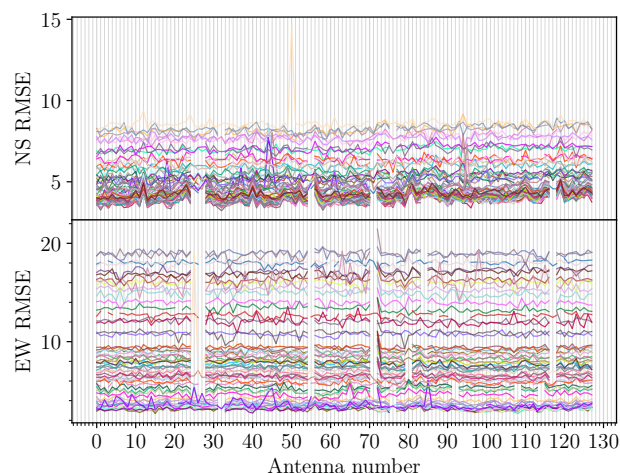


**Figure 23.** RMSE metric for both NS and EW cross polarisations for the HERA LST 5.2 field. Each line is a different observation. A value closer to 0 is ideal, and indicates more linear phase solutions.

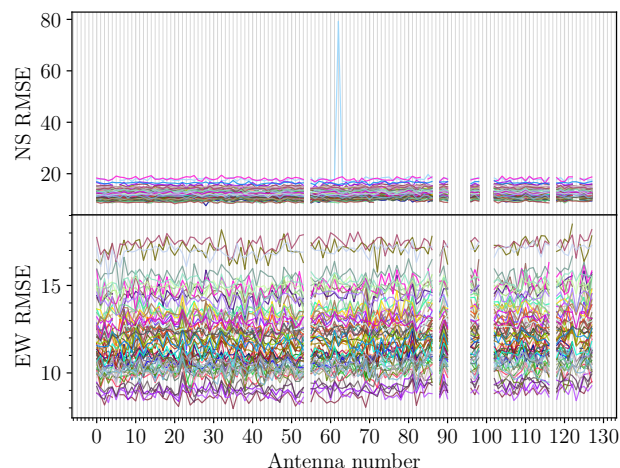


**Figure 24.** RMSE metric for both NS and EW cross polarisations for the SKAEOR5 field. Each line is a different observation. A value closer to 0 is ideal, and indicates more linear phase solutions.

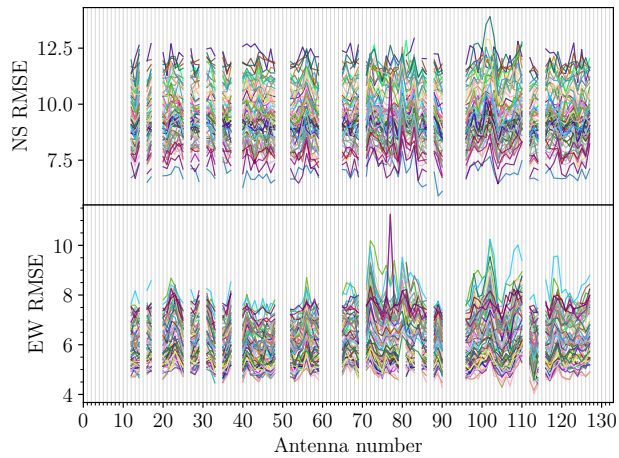


**Figure 25.** RMSE metric for both NS and EW cross polarisations for the SKAEOR15 field. Each line represents a different observation. A value closer to 0 is ideal, and indicates more linear phase solutions.

#### Appendix 5. Average Euclidean distance metric

This appendix contains figures for the calibration phase average Euclidean distance metric for the HERA LST 5.2, SKAEOR5, and SKAEOR15 fields.

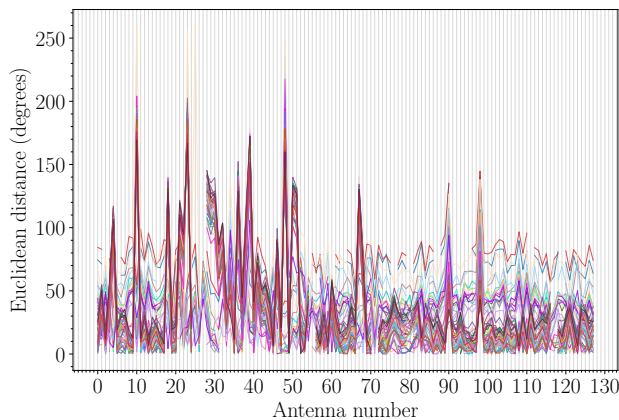


**Figure 26.** The average Euclidean distance between the NS and EW cross polarisations for each antenna in each observation for the HERA LST 5.2 field. A value closer to 0 is ideal and signals that the solutions are more similar.

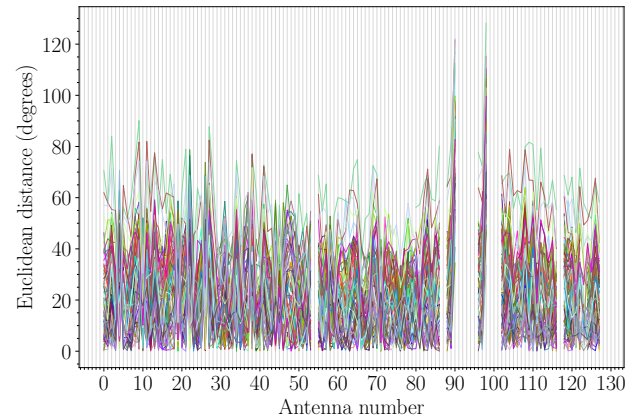


**Figure 27.** The Euclidean distance between the NS and EW cross polarisations for each antenna in each observation for the SKAEOR5 field. A value closer to 0 is ideal and signals that the solutions are more similar.

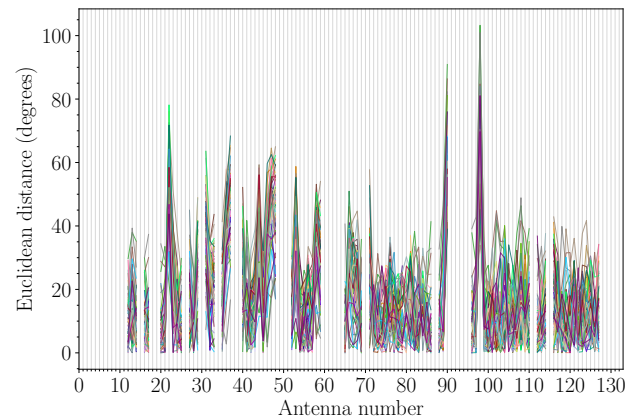


**Figure 28.** The Euclidean distance between the NS and EW cross polarisations for each antenna in each observation for the SKAEOR15 field. A value closer to 0 is ideal and signals that the solutions are more similar.